

Improved Chest Anomaly Localization without Pixel-level Annotation via Image Translation Network Application in Pseudo-paired Registration Domain

Kyungsu Kim^{1,2*†}, Seong Je Oh^{3*}, Tae Uk Kim⁴, Myung Jin Chung^{1,2,4,5†}

¹Medical AI Research Center, Research Institute for Future Medicine, Samsung Medical Center, Seoul, Korea

²Department of Data Convergence and Future Medicine, Sungkyunkwan University School of Medicine, Seoul, Korea

³Department of Health Sciences and Technology, SAIHST, Sungkyunkwan University, Seoul, Korea

⁴Department of Digital Health, SAIHST, Sungkyunkwan University, Seoul, Korea

⁵Department of Radiology, Samsung Medical Center, Sungkyunkwan University School of Medicine, Seoul, Korea

Abstract

Image translation based on a generative adversarial network (GAN-IT) is a promising method for the precise localization of abnormal regions in chest X-ray images (AL-CXR) even without pixel-level annotation. However, heterogeneous unpaired datasets undermine existing methods to extract key features and distinguish normal from abnormal cases, resulting in inaccurate and unstable AL-CXR. To address this problem, we propose an improved two-stage GAN-IT involving registration and data augmentation. For the first stage, we introduce an advanced deep-learning-based registration technique that virtually and reasonably converts unpaired data into paired data for learning registration maps, by sequentially utilizing linear-based global and uniform coordinate transformation and AI-based non-linear coordinate fine-tuning. This approach enables the independent and complex coordinate transformation of each detailed location of the lung while recognizing the entire lung structure, thereby achieving higher registration performance with resolving inherent artifacts caused by unpaired conditions. For the second stage, we apply data augmentation to diversify anomaly locations by swapping the left and right lung regions on the uniform registered frames, further improving the performance by alleviating imbalance in data distribution showing left and right lung lesions. The proposed method is model agnostic and shows consistent AL-CXR performance improvement in representative AI models. Therefore, we believe GAN-IT for AL-CXR can be clinically implemented by using our basis framework, even if learning data are scarce or difficult for the pixel-level disease annotation.

1 Introduction

Chest X-ray (CXR) imaging is used as a first-line test for identifying lung anomalies because it provides fast image generation with a low radiation dose [1]. However, it is difficult to accurately diagnose diseases under fine shading conditions. Existing systems and methods should be further improved as precise anomaly localization in CXR images (AL-CXR) are clinically important. The recent application of deep

*Equal contribution

†Corresponding author: Kyungsu Kim (kskim.doc@gmail.com) and Myung Jin Chung (mjchung@skku.edu)

learning (DL) to CXR diagnosis has substantially improved the detection of anomalies in patients [2, 3, 4]. Nevertheless, apart from simple discrimination, this approach does not guarantee the precise identification of subregions with anomalies. Although class activation maps and their variants have been typically used to achieve AL-CXR, they have limited resolution in blurry maps and show clinical limitations regarding interpretation (e.g., it is difficult to obtain normal class activation in a disease-free region).

Generative adversarial network (GAN)-based image translation (GAN-IT) establishes an alternative for detecting abnormal regions in CXR images because it supports high-resolution outputs by applying adversarial learning. It converts real CXR images containing disease regions into normal CXR images, and it has been used to specify abnormal regions in the lung using the differences between the images. Although GAN-IT is promising for AL-CXR, stability and accuracy require further improvement. GAN-IT for AL-CXR has a low performance because learning is performed using unpaired data (i.e., normal/abnormal image pairs taken in different environments from different patients—unpaired, not normal/abnormal image pairs taken under the same conditions of the same patient—paired). For pixel-level AL-CXR, even a small spatial difference between the input and labeled images (e.g., target images before and after translation) notably affects image translation. Therefore, the possible structural mismatch of relative positions in images from unpaired datasets during registration learning may considerably degrade performance.

To improve GAN-IT for AL-CXR, we propose a model-agnostic method called image translation under pseudo-paired registration with bilaterally symmetrical data augmentation (IT-PRBA) and an extension of its registration to DL (IT-DPRBA). Both methods aim to improve the AL-CXR performance through a novel registration technique for pre/postprocessing in conventional GAN-IT models.

The proposed IT-PRBA has a unique and reversible registration without requiring DL network training and generates a coordinate transformation map (i.e., the lung image of a moving patient is fit to a fixed lung region) using only a fixed lung mask. As the proposed registration generates a pseudo-paired (i.e., moving/fixed) dataset with only moving images without applying DL, we call it DL-free pseudo-pair registration (DLF-PR). IT-DPRBA extends IT-PRBA through DL-based registration using a paired dataset obtained by DLF-PR, whereas trained registration instead of DLF-PR is used in IT-PRBA. The DL-based method is called DL-based pseudo-paired registration (DL-PR). Unlike existing DL-based registration techniques that simply learn an unpaired dataset [5, 6], the registration in the proposed IT-DPRBA learns a virtual and reasonable paired dataset. This is because the obtained pseudo-paired dataset is less affected by artifacts owing to variations in an unpaired dataset, thereby facilitating finetuning of detailed deformable positions under a virtual and reasonable paired domain in a registration network. The advanced DLF-PR and DL-PR allow GAN-IT to learn relations between abnormal and normal data in a unified domain. Therefore, regions corresponding to diseases in CXR lung images can be easily learned even with a small training set.

In IT-PRBA and IT-DPRBA, we introduce bilaterally symmetrical data augmentation (BA), which further improves the performance of GAN-IT for AL-CXR by addressing data imbalance in CXR images containing left/right lung lesions. BA converts an image of the left (right) lung into that of the right (left) lung at the pixel level in the standardized/registered domain. It effectively augments disease data by creating a hypothetical patient with a disease on the other side from a patient with a disease in only one of the left and right lungs. BA is easily implemented owing to the reversible nature of the proposed registration techniques.

We evaluated IT-PRBA and IT-DPRBA by integrating them into state-of-the-art GAN-IT models, namely, CycleGAN [7] and contrastive unpaired translation (CUT) [8]. We observed that the AL-CXR performance (e.g., for tuberculosis or consolidation shadow cases) is considerably improved when applying our proposal. The source code is available at <https://github.com/kskim-phd/IT-DPRBA>.

2 Related Work

2.1 GAN-based Anomaly Localization

A GAN is a representative DL architecture to synthesize training sets. It can transform unlearned data into samples within learned data. Schlegl et al. [9] showed that unsupervised learning with GANs using only training data from normal patients allows creating a virtual normal image from the actual image of a patient with anomalies, identifying the abnormal region using the difference between images. Subsequent studies have been conducted to accelerate processing [10], improve performance [11, 12, 13], and apply this method to CXR images [14, 15, 16]. However, unsupervised learning may generate images with high deviations and unstable anomaly localization [17].

Weakly supervised GANs based on training with both normal and abnormal labeled data have recently been adopted to further improve performance. In addition to exploiting abnormal data during learning, such GANs outperform those based on unsupervised learning for accurate anomaly localization and stability [18, 19, 20]. In principle, these methods are based on image translation [21, 22], which synthesizes normal CXR images from CXR images containing disease regions. However, existing GAN- or GAN-IT-based methods for anomaly localization neglect the performance enhancement achievable using registration for learning. In contrast, we explore registration for integration into image translation models as a pre/postprocessing stage aiming to further improve the AL-CXR performance.

2.2 GAN-based Image Translation

Various GANs for general image translation have been proposed [7, 8, 23, 24, 25, 26, 27]. Zhu et al. [7] first demonstrated that image translation can be performed by bidirectionally connecting two GANs in a CycleGAN. Subsequent studies [8, 23, 27, 26] addressed the structural imbalance between images before and after translation by enhancing the recognition of spatial location information in image feature maps through contrastive learning. A representative model of this approach is CUT [8]). Another follow-up study on CycleGAN was aimed to enhance the conversion performance by separating style information of an image or applying artificial distortion to an image [24, 25]. Unlike our study, these previous developments neglected registration between unpaired images for learning image translation.

2.3 Registration-based Image Translation

Recent GAN-IT models have been developed to improve the IT performance by adopting the deformable registration [28, 29, 30, 31]. Arar et al. [28] selectively added a registration network to the input or output of a GAN-IT model, thereby improving the image translation performance by simultaneously learning the translation and registration models. Kong et al. [29] improved the GAN-IT performance by applying data augmentation to introduce random noise for coordinate transformation through registration. Yang et al. [30] demonstrated the contribution of registration to GAN-IT for relating different modalities. Chen et al. [31] used registration and GAN-IT and removed the GAN discriminator to improve performance. However, unlike our study, the aforementioned existing studies that used registration to IT did not progress registration itself. Specifically, they did not provide an enhanced registration strategy that explicitly addresses the issue of disease artifact fabrication resulting from unpaired data during registration training. In contrast, we use the novel DLF-PR to convert an unpaired dataset into a paired one and propose DL-PR that can be trained with this virtually paired dataset. This effects as alleviating the artifact generation issue, thereby improving both registration and unpaired IT performance.

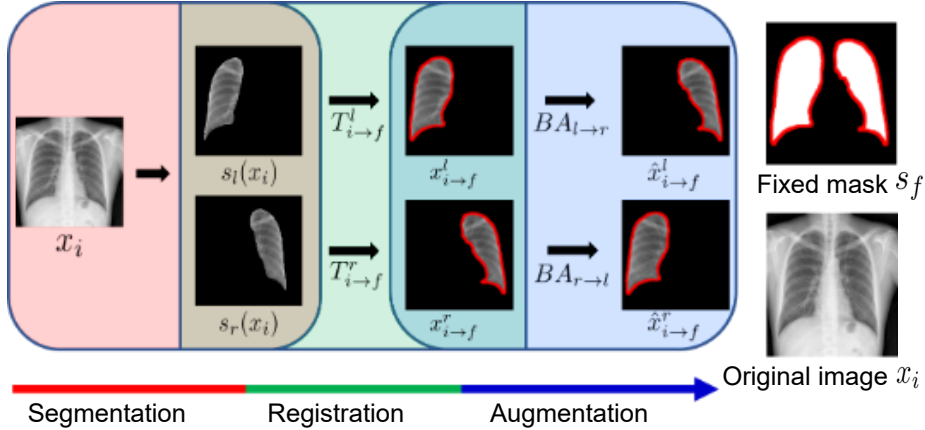


Figure 1: Process of IT-PRBA/IT-DPRBA.

3 Methods

3.1 Image translation

We consider image translation from input domain $X \subset \mathbb{R}^{h \times w}$ to output domain $Y \subset \mathbb{R}^{h \times w}$. We provide a training dataset for unpaired instances $X = \{x \in \mathcal{X}\}$ and $Y = \{y \in \mathcal{Y}\}$. Image translation aims to parameterize mapping K_θ satisfying $K_\theta : X \mapsto Y$. This task can be formulated to determine optimal parameter θ^* of a translation model as follows:

$$\theta^* = \operatorname{argmin}_\theta |I(X, \hat{Y}_\theta(X)) - I(X, Y)|, \quad (1)$$

where I denotes the mutual information and $\hat{Y}_\theta(X) := \{K_\theta(x) \mid x \in X\}$ denotes the model translation result for X .

3.2 Baseline GAN-IT for AL-CXR

Consider n lung CXR images from patients with anomalies and let the indices and dataset be $\{1 : n\} := \{1, 2, \dots, n\}$ and $X = \{x_i\}_{i \in \{1:n\}}$, respectively. In addition, consider m lung CXR images from healthy patients with index and datasets denoted as $\{1 : m\}$ and $Y = \{y_i\}_{i \in \{1:m\}}$, respectively. From the learning data, we train the model using (1) and perform AL-CXR by identifying anomaly map v_t as the difference between test CXR image x_t (normal or abnormal) and its synthesized result $\hat{y}_t = K_{\theta^*}(x_t)$ as follows:

$$v_t = x_t \odot \operatorname{SEG}_{\psi^*}(x_t) - \hat{y}_t \odot \operatorname{SEG}_{\psi^*}(\hat{y}_t), \quad (2)$$

where $\operatorname{SEG}_{\psi^*}$ denotes a pretrained segmentation network that extracts the inner region of the lung as a binary mask. The left- and right-hand terms in (2) refer to the modified CXR images of x_t and \hat{y}_t , respectively, in which the outer lung region is set to zero.

3.3 Proposed IT-PRBA

The proposed IT-PRBA comprises three stages: segmentation, registration, and BA. These stages are described in Algorithm 1 and Fig. 1.

Algorithm 1 IT-PRBA

1: Segmentation stage**Input:** x_i for $i \in \{1 : n\}$, $\text{SEG}_{\theta^*} : \mathbb{R}^{h \times w} \mapsto \mathbb{R}^{h \times w}$

- 1: **for** $i = 1$ to n **do**
- 2: $s_i \leftarrow \text{SEG}_{\psi^*}(x_i)$
- 3: $(s_i^l, s_i^r) \leftarrow \text{split}(s_i)$
- 4: $(s^l(x_i), s^r(x_i)) \leftarrow (s_i^l \odot x_i, s_i^r \odot x_i)$
- 5: **end for**

Output: Left and right lung binary masks (s_i^l, s_i^r) and their inner images $(s^l(x_i), s^r(x_i))$ for patient i ($i \in \{1 : n\}$)

2: Registration stage**Input:** x_i, s_i^l , and s_i^r for $i \in \{1 : n\}$

- 1: **for** $i = 1$ to n **do**
- 2: $(T_{i \rightarrow f}^l, T_{f \rightarrow i}^l) \leftarrow \text{REG}(s_i^l, s_f^l)$
- 3: $(T_{i \rightarrow f}^r, T_{f \rightarrow i}^r) \leftarrow \text{REG}(s_i^r, s_f^r)$
- 4: $(x_{i \rightarrow f}^l, x_{i \rightarrow f}^r) \leftarrow (T_{i \rightarrow f}^l(s^l(x_i)), T_{i \rightarrow f}^r(s^r(x_i)))$
- 5: **end for**

 \triangleright Moving original (x_i^l, x_i^r) to reference (x_f^l, x_f^r) **Output:** Moved left $x_{i \rightarrow f}^l$ and right $x_{i \rightarrow f}^r$ lung images of patient i

3: Augmentation stage**Input:** $x_{i \rightarrow f}^l, x_{i \rightarrow f}^r, s_i^l$, and s_i^r for $i \in \{1 : n\}$

- 1: **for** $i = 1$ to n **do**
- 2: $(\hat{x}_{i \rightarrow f}^l, \hat{x}_{i \rightarrow f}^r) \leftarrow (\text{BA}_{r \rightarrow l}(x_{i \rightarrow f}^r, s_f^l), \text{BA}_{l \rightarrow r}(x_{i \rightarrow f}^l, s_f^r))$
- 3: **end for**

Output: Augmented (synthesized) left lung $\hat{x}_{i \rightarrow f}^l$ and right lung $\hat{x}_{i \rightarrow f}^r$ images of patient i

3.3.1 Segmentation

Segmentation of CXR image x_i extracts the left (s_i^l) and right (s_i^r) lung binary masks and leaves only the region inside the left ($s^l(x_i)$) and right ($s^r(x_i)$) lung images, as shown in Fig. 1. The binary masks are obtained by splitting the entire mask given as the pretrained segmentation model output, $\text{SEG}_{\theta^*}(\cdot)$. Then, left ($s^l(x_i)$) and right ($s^r(x_i)$) lung images are obtained by elementwise multiplication \odot of each mask (s^l, s^r) by x_i .

3.3.2 Registration without DL

We propose a DL-free registration method and its extension using DL. We first describe DLF-PR; DL-PR is introduced in Section 3.5. DLF-PR calculates coordinate shift functions $T_{i \rightarrow f}^l$ and $T_{i \rightarrow f}^r$ mapping from left (s_i^l) and right (s_i^r) lung masks to those of a fixed lung mask s_f , where i and f indicate patient i and fixed, respectively.

To obtain the corresponding maps, we introduce a coordinate domain to convert general coordinate values $(\alpha, \beta) \in \mathbb{R}^2$ of horizontal/vertical axes at a specific position in a CXR image into relative position coordinates in the lung internal region (inside lung mask s) as $C_s(\alpha, \beta) \in [0, 1]^4$:

$$C_s(\alpha, \beta) := \left(\frac{p_1^s}{p_1^s + p_2^s}, \frac{p_2^s}{p_1^s + p_2^s}, \frac{q_1^s}{q_1^s + q_2^s}, \frac{q_2^s}{q_1^s + q_2^s} \right). \quad (3)$$

Examples using $C_s(\alpha, \beta)$ are shown in Fig. 2. We obtain the longest line starting from the lowest (red) point of each left and right lung, set this line as a new vertical axis and define a perpendicular horizontal

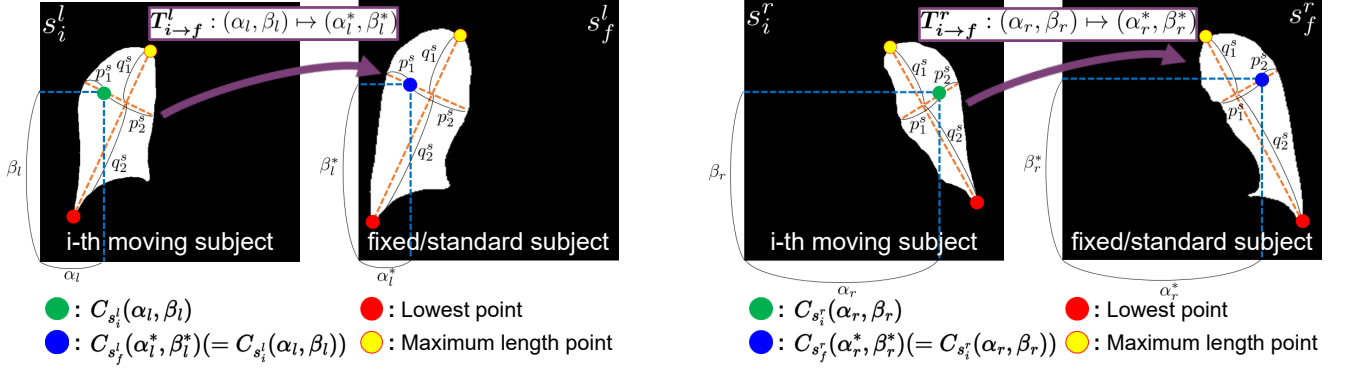


Figure 2: Diagram of proposed DLF-PR process.

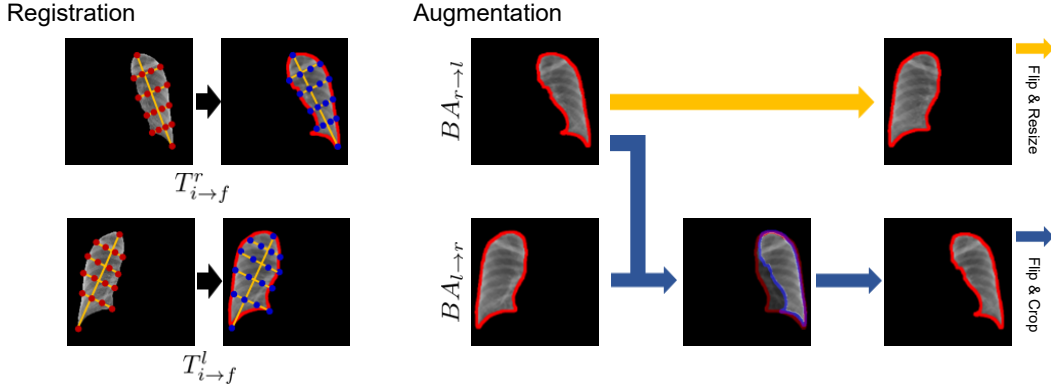


Figure 3: Key characteristics of registration and augmentation in IT-PRBA.

axis, and transform original coordinates $(\alpha, \beta) \in \mathbb{R}^2$ into coordinates $C_s(\alpha, \beta) \in [0, 1]^4$, which are described by the relative position inside the lung expressed between 0 and 1 along the new horizontal and vertical axes.

Considering relative coordinate domain $C_s(\alpha, \beta)$, we obtain coordinate shift function $T_{i \to f}$ such that it maps corresponding relative coordinates $C_{s_i}(\alpha, \beta)$ of the moving patient's lung mask, s_i , to be the same as the corresponding relative coordinates, $C_{s_f}(\alpha, \beta)$, of the fixed patient's lung mask, s_f . Particularly, the function can be formulated using (5) and (7) for each lung on the left and right sides, respectively:

$$T_{i \to f}^l := \{(\alpha, \beta) \mapsto (\alpha_l^*, \beta_l^*) \mid \forall (\alpha, \beta) \in \text{supp}(s_i^l)\}, \quad (4)$$

$$(\alpha_l^*, \beta_l^*) := \underset{(\alpha', \beta') \in \text{supp}(s_f^l)}{\text{argmin}} \left\| C_{s_i^l}(\alpha, \beta) - C_{s_f^l}(\alpha', \beta') \right\|, \quad (5)$$

$$T_{i \to f}^r := \{(\alpha, \beta) \mapsto (\alpha_r^*, \beta_r^*) \mid \forall (\alpha, \beta) \in \text{supp}(s_i^r)\}, \quad (6)$$

$$(\alpha_r^*, \beta_r^*) := \underset{(\alpha', \beta') \in \text{supp}(s_f^r)}{\text{argmin}} \left\| C_{s_i^r}(\alpha, \beta) - C_{s_f^r}(\alpha', \beta') \right\|, \quad (7)$$

where s_i^l and s_i^r indicate the left and right lung binary masks of patient i , respectively and supp denotes the support set (i.e., nonzero index/location set). Therefore, the value of (α^*, β^*) corresponds to the position in the reference lung with respect to the coordinates of (α, β) (i.e., the relative position inside the lung becomes the same).

Algorithm 2 Training

Training for baseline**Input:** $X = \{x_i\}_{i \in \{1:n\}}, Y = \{y_i\}_{i \in \{1:m\}}, K_\theta$ 1: $\theta^* \leftarrow \operatorname{argmin}_\theta |I(X, \hat{Y}_\theta(X)) - I(X, Y)|$ **Output:** Trained model K_{θ^*}

Training for proposed method using IT-PRBA**Input:** X_r, X_l, Y_r, Y_l given by (8), $K_{\theta_r}, K_{\theta_l}$ 1: $\theta_r^* \leftarrow \operatorname{argmin}_{\theta_r} |I(X_r, \hat{Y}_{\theta_r}(X_r)) - I(X_r, Y_r)|$ 2: $\theta_l^* \leftarrow \operatorname{argmin}_{\theta_l} |I(X_l, \hat{Y}_{\theta_l}(X_l)) - I(X_l, Y_l)|$ **Output:** Trained models $K_{\theta_r^*}$ and $K_{\theta_l^*}$

Algorithm 3 Testing

Test of baseline**Input:** Test CXR image x_t, K_{θ^*} 1: $\hat{y}_t \leftarrow K_{\theta^*}(x_t)$ **Output:** Synthesized normal CXR image \hat{y}_t translated from target CXR image x_t

Testing of proposed method using IT-PRBA**Input:** Test CXR image $x_t, K_{\theta_r^*}, K_{\theta_l^*}$ 1: $(x_{t \rightarrow f}^l, x_{t \rightarrow f}^r) \leftarrow$ perform up to step 4 of registration by replacing x_i with x_t 2: $\hat{y}_t^l \leftarrow T_{f \rightarrow t}^l(s_l(K_{\theta_r^*}(x_{t \rightarrow f}^l)))$ 3: $\hat{y}_t^r \leftarrow T_{f \rightarrow t}^r(s_r(K_{\theta_l^*}(x_{t \rightarrow f}^r)))$ 4: $\hat{y}_t \leftarrow s_t^l \odot \hat{y}_t^l + s_t^r \odot \hat{y}_t^r + (1 - s_t^l) \odot x_t$ **Output:** Synthesized normal CXR image \hat{y}_t translated from target CXR image x_t

Then, we also define the inverse maps of $T_{i \rightarrow f}^l$ and $T_{i \rightarrow f}^r$ as $T_{f \rightarrow i}^l$ and $T_{f \rightarrow i}^r$, respectively. They map transformed coordinates (α^*, β^*) onto original coordinates (α, β) . The transformation maps $(T_{i \rightarrow f}, T_{f \rightarrow i})$ between the lung images of moving and fixed patients can be obtained only from the mask information of the patients, s_i and s_f . Hence, the generation of these maps given by (4) and (6) can be compactly expressed as function REG:

$$(T_{i \rightarrow f}^l, T_{f \rightarrow i}^l) \leftarrow \operatorname{REG}(s_i^l, s_f^l), (T_{i \rightarrow f}^r, T_{f \rightarrow i}^r) \leftarrow \operatorname{REG}(s_i^r, s_f^r).$$

The role of these maps is illustrated in Fig. 3. We find the longest vertical line (e.g., yellow vertical lines in Fig. 3) from the lowest point on the outer edge of each lung image and derive a vertical grid that equally divides the vertical line into various intervals. Then, we obtain each horizontal line (e.g., yellow horizontal lines in Fig. 3) that includes each vertical grid perpendicular to the vertical line and derive a horizontal grid that equally divides the horizontal line into various intervals. Then, maps $T_{i \rightarrow f}^l$ and $T_{i \rightarrow f}^r$ are obtained by linearly transforming each point on the grid (e.g., red point for registration in Fig. 3) into a point (e.g., blue point for registration in Fig. 3) obtained by applying the same process to fixed lung mask s_f . To fit the registered images to the original images, we obtain inverse coordinate shift maps $T_{f \rightarrow i}^l$ and $T_{f \rightarrow i}^r$. Additional implementation details for REG are provided in Appendix (Algorithm 4).

Through registration, the relative position inside the lungs of all patients is fixed at specific coordinates. This facilitates learning of image translation using a GAN, even on a small dataset. We demonstrate the effectiveness of the proposed registration compared with existing technologies in Sections 3.5 and 4.5.

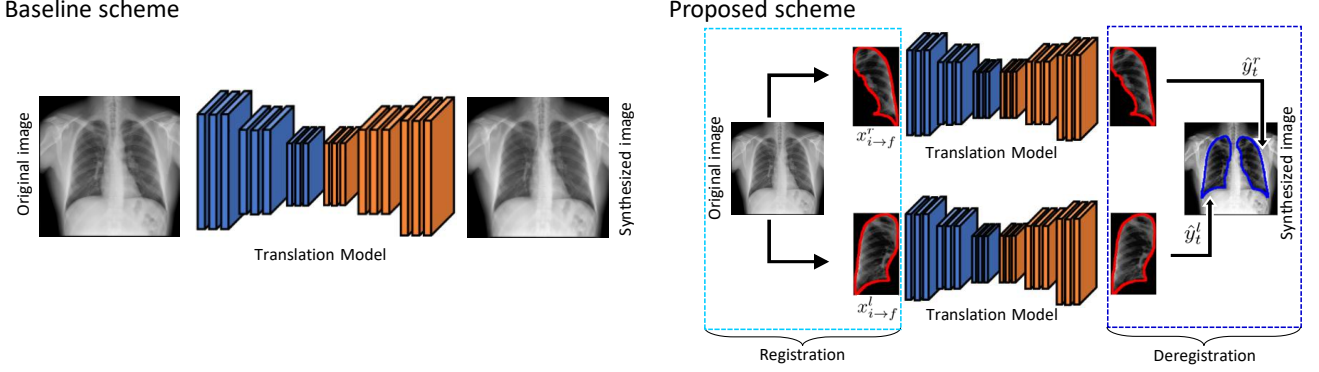


Figure 4: Testing: proposed IT-PRBA (or IT-DPRBA) compared with baseline GAN-IT.

3.3.3 Training data augmentation by BA

The proposed BA doubles the number of images by generating opposite (i.e., right and left) lung images from left and right fixed lung images $x_{i \rightarrow f}^l$ and $x_{i \rightarrow f}^r$ as $\hat{x}_{i \rightarrow f}^l$ and $\hat{x}_{i \rightarrow f}^r$, respectively. Because the right lung image has a horizontally narrower lung region owing to the presence of the heart, after flipping the left image to the right, we partially remove the virtual heart region of the flipped image to fit the right lung (i.e., right lung region excluding the heart), as shown in Fig. 3 (blue arrow). Details for proposed BA are provided in Appendix (Algorithm 5).

3.4 Application of IT-PRBA to GAN-IT for AL-CXR

3.4.1 Training

Algorithm 2 describes model training using a baseline method and the proposed IT-PRBA. We set the baseline as detailed in Section 3.2. In place of the input and label data used in the baseline, we use input data X_l and X_r and label data Y_l and Y_r for the left and right lungs, respectively, in the IT-PRBA as follows. From step 2 in the augmentation stage of Algorithm 1, we obtain

$$\begin{aligned}
 X_r &= \{s_r(x_{i \rightarrow f}^r)\}_{i \in \{1:n\}} \cup \{s_r(\hat{x}_{i \rightarrow f}^r)\}_{i \in \{1:n\}}, \\
 X_l &= \{s_l(x_{i \rightarrow f}^l)\}_{i \in \{1:n\}} \cup \{s_l(\hat{x}_{i \rightarrow f}^l)\}_{i \in \{1:n\}}, \\
 Y_r &= \{s_r(y_i)\}_{i \in \{1:m\}}, \\
 Y_l &= \{s_l(y_i)\}_{i \in \{1:m\}}.
 \end{aligned} \tag{8}$$

The number of abnormal samples in X_r or X_l is twice that in X after applying the proposed augmentation. Thus, the amount of data can be considerably increased using our method in a clinical environment in which abnormal (e.g., disease) cases are scarce.

3.4.2 Testing

Algorithm 3 describes model testing using the baseline and proposed IT-PRBA. Typical baseline image translation methods use original CXR image x_t as the input. However, in the method in which the proposed IT-PRBA is applied, registered image $x_{t \rightarrow f}$ of x_t is used as the input. Subsequently, uniform output $K_{\theta^*}(x_{t \rightarrow f})$ is provided and expressed back in the original image coordinates as $\hat{y}_t = T_{f \rightarrow t}(s_l(K_{\theta^*}(x_{t \rightarrow f})))$.

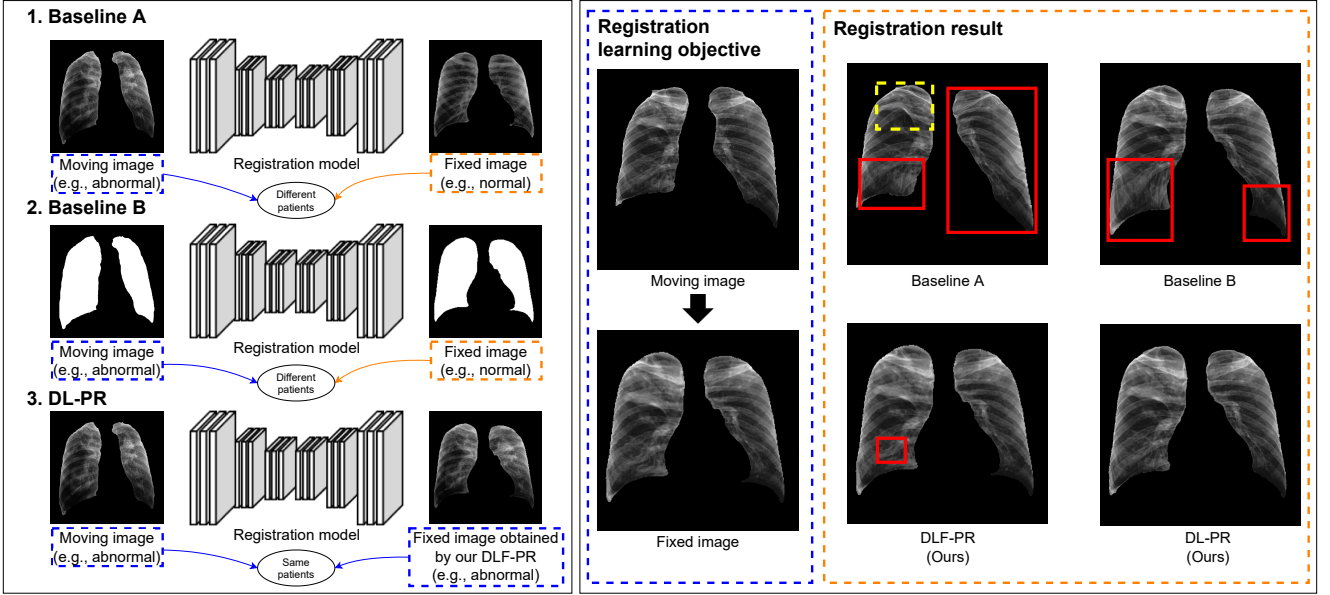


Figure 5: Diagram of proposed DL-PR. Other DL-based baseline techniques (A and B) are unpaired regarding moving and fixed images, impeding proper registration learning (i.e., disease distortion and lung area artifacts as shown in yellow and red boxes respectively). In contrast, DL-PR secures paired (moving/fixed) learning data for the same patient/image source by generating fixed images from moving ones via DLF-PR.

Finally, anomaly map v_t is given by (2) from \hat{y}_t , where v_t represents the difference in the image information between the original image and virtual normal image generated by the network. In other words, the proposed method allows advanced anomaly localization by performing image translation in the registered domain. This process is performed as a separate network (i.e., $K_{\theta_l^*}$ and $K_{\theta_r^*}$) for the left and right lungs (steps 2 and 3), and the results are combined during deregistration (step 4 in Algorithm 3), as illustrated in Fig. 4.

3.5 IT-DPRBA: DL-based extension of IT-PRBA

The proposed DLF-PR performs registration using coordinate transformation function $T_{i \rightarrow f}$ given by (4) and (6). The transformation allows the lung region mask of each moving patient to be uniformly mapped onto a reference mask. Hence, a formable instead of deformable coordinate transformation is obtained; however, it cannot achieve perfect lung region coordinate transformation. We address this problem using the proposed DL-PR, which is applicable to any DL-based registration network. Unlike conventional DL-based registration, which uses the learning label as a fixed image, the proposed DL-PR considers a label from a moving image using the DLF-PR output for learning. In other words, existing DL-based registration uses data from different moving and fixed patients, leading to identification of inexistent diseases in images from healthy moving patients and fixed patients with diseases. Conversely, the proposed DL-PR avoids this problem by learning registration using moving and fixed (i.e., result from DLF-PR) images of the same patient. Fig. 5 shows the differences between DL-PR and existing DL-based registration techniques for learning and the different registration performances. For an accurate comparison, the proposed and existing DL-based registration techniques are formulated in detail as follows.

Proposed DL-based registration technique For training of the proposed DL-PR, given a registration network REG_ϕ with training parameter ϕ , the network takes moving image x_m as its input and learns to output pseudo-label $T_{m \rightarrow f}(x_m)$, which is the moved image generated by DLF-PR. The learning objective is given by

$$\phi_{i \rightarrow f}^{l*} := \operatorname{argmin}_{\phi_{i \rightarrow f}^l} \mathcal{L}_{\phi_{i \rightarrow f}^l} \left(REG_{\phi_{i \rightarrow f}^l} (s^l(x_i)), T_{i \rightarrow f}^l(s^l(x_i)) \right), \quad (9)$$

$$\phi_{i \rightarrow f}^{r*} := \operatorname{argmin}_{\phi_{i \rightarrow f}^r} \mathcal{L}_{\phi_{i \rightarrow f}^r} \left(REG_{\phi_{i \rightarrow f}^r} (s^r(x_i)), T_{i \rightarrow f}^r(s^r(x_i)) \right), \quad (10)$$

where $\mathcal{L}_\phi(a, b)$ denotes a training loss (e.g., mean squared error) for DL-based registration with network input a (moving image) and label b (fixed image), $s^l(x_i)$ and $s^r(x_i)$ denote the left and right lung images of the moving patient i , and $T_{i \rightarrow f}^l(s^l(x_i))$ and $T_{i \rightarrow f}^r(s^r(x_i))$ denote their lung images moved using IT-PRBA.

From learning described in (9) and (10), we can obtain smoother/more deformable coordinate transformation functions $\hat{T}_{i \rightarrow f}^l$ and $\hat{T}_{i \rightarrow f}^r$ (i.e., results by DL-PR) than those provided by DLF-PR (i.e., $T_{i \rightarrow f}^l$ and $T_{i \rightarrow f}^r$); proposed DL-PR calculates coordinate shift functions $\hat{T}_{i \rightarrow f}^l$ and $\hat{T}_{i \rightarrow f}^r$ mapping from left (s_i^l) and right (s_i^r) lung masks to those of a fixed lung mask s_f as the output results of following trained registration networks, where i and f indicate patient i and fixed, respectively:

$$\hat{T}_{i \rightarrow f}^l := REG_{\phi_{i \rightarrow f}^{l*}}, \quad \hat{T}_{i \rightarrow f}^r := REG_{\phi_{i \rightarrow f}^{r*}},$$

and DL-PR also provides their inverse maps as $\hat{T}_{f \rightarrow i}^l$ and $\hat{T}_{f \rightarrow i}^r$, respectively.

Accordingly by using DL-PR, we propose an extension of IT-PRBA called IT-DPRBA, which converts all coordinate transformation functions $T_{i \rightarrow f}^l$, $T_{i \rightarrow f}^r$, $T_{f \rightarrow i}^l$, and $T_{f \rightarrow i}^r$ into $\hat{T}_{i \rightarrow f}^l$, $\hat{T}_{i \rightarrow f}^r$, $\hat{T}_{f \rightarrow i}^l$, and $\hat{T}_{f \rightarrow i}^r$, respectively, in the testing phase of GAN-IT as described in Section 3.4.2 (Algorithm 3). That is, AL-CXR can be performed by applying IT-DPRBA to GAN-IT through the same approach of IT-PRBA by replacing only the coordinate transformation function. This modification from IT-PRBA to IT-DPRBA provides more stable image registration as evaluated in Section 4.5, thereby achieving better anomaly localization performance as shown in Tables 7 and 8 in Section 4.4.2.

Existing DL-based registration techniques (Baselines A and B) Unlike the DL-PR objective given by (9) and (10), conventional DL-based registration aims to optimize parameter ψ as ψ^* and obtain coordinate transformation functions $\hat{T}_{i \rightarrow f}^l := REG_{\psi_{i \rightarrow f}^{l*}}$ and $\hat{T}_{i \rightarrow f}^r := REG_{\psi_{i \rightarrow f}^{r*}}$:

$$\psi_{i \rightarrow f}^{l*} := \operatorname{argmin}_{\psi_{i \rightarrow f}^l} \mathcal{L}_{\psi_{i \rightarrow f}^l} \left(REG_{\psi_{i \rightarrow f}^l} (s^l(x_i)), s^l(x_f) \right), \quad (11)$$

$$\psi_{i \rightarrow f}^{r*} := \operatorname{argmin}_{\psi_{i \rightarrow f}^r} \mathcal{L}_{\psi_{i \rightarrow f}^r} \left(REG_{\psi_{i \rightarrow f}^r} (s^r(x_i)), s^r(x_f) \right), \quad (12)$$

where $s^l(x_i)$ and $s^r(x_i)$ ($s^l(x_f)$ and $s^r(x_f)$) denote the left and right lung images of the moving (fixed) patient, respectively. Training given by (11) and (12) is called DL-based registration baseline A. Baseline A uses image x_f of a patient different from image x_i of a moving patient as a label (i.e., $s^l(x_f)$ and $s^r(x_f)$). This unpaired nature results in unintended disease reduction or distortion artifacts in moved/registered images if the fixed image for training has no disease but the moving image for training has a disease. However, our technique described by (9) and (10) uses the label (fixed) image, whose patient information with image content and structure is the same as that of a moving patient image x_i . Hence, in DL-PR,

the training difference between moving and fixed images exists only for coordinate information, thereby ensuring more reliability for registration learning (i.e., Our DL-PR makes a moving patient being registered to a fixed patient paired with the same moving patient, thereby solving disease reduction or distortion artifacts that baseline A may suffer.).

We also consider another learning objective for DL-based registration in registration baseline B. Unlike baseline A given by (11) and (12), baseline B uses only binary lung mask information (i.e., s_i and s_f) depending on whether it belongs to the lung, without exploiting internal lung information, $s(x_i)$ and $s(x_f)$, of moving and fixed patients, respectively. Baseline B optimizes parameter π as π^* and obtains coordinate transformation functions $\hat{T}_{i \rightarrow f}^l := REG_{\pi_{i \rightarrow f}^{l*}}$ and $\hat{T}_{i \rightarrow f}^r := REG_{\pi_{i \rightarrow f}^{r*}}$ as follows:

$$\pi_{i \rightarrow f}^{l*} := \operatorname{argmin}_{\pi_{i \rightarrow f}^l} \mathcal{L}_{\pi_{i \rightarrow f}^l} \left(REG_{\pi_{i \rightarrow f}^l} (s_i^l), s_f^l \right), \quad (13)$$

$$\pi_{i \rightarrow f}^{r*} := \operatorname{argmin}_{\pi_{i \rightarrow f}^r} \mathcal{L}_{\pi_{i \rightarrow f}^r} \left(REG_{\pi_{i \rightarrow f}^r} (s_i^r), s_f^r \right). \quad (14)$$

In this case of baseline B, unlike baseline A, no artifacts such as anomaly reduction or distortion are generated after registration because the pixel values on the inner region of the lung for both moving and fixed images are the same as 1. However, proper registration fails because the relative position between the coordinates after registration is not uniform, resulting in an unrealistic scenario. This is because during training of baseline B, the intersecting coordinate region, in which the binary masks of the moving and fixed patients are with a value of 1, shows slight motion compared with other regions.

As shown in Fig. 5 (and Fig. 7), the proposed DL-PR overcomes limitations of baselines A and B (yellow and red boxes in Figs. 5 and 7 respectively). In fact, DL-PR creates a moving/fixed training pair for the same patient to suppress artifacts influencing baseline A and solves the nonuniform registration of baseline B using information of the lung internal structure rather than a simple binary mask.

4 Experiments and Results

4.1 Data preparation

We used a publicly available dataset [32] that provides an anomaly of tuberculosis as a boundary box. From each of the first part of the class sets of abnormal (i.e., tuberculosis) and normal of this data set, we selected 600 samples for training ($n, m = 600$), and the remaining 150 and 758 samples for testing, respectively. In addition to tuberculosis, we collected 750 cases of consolidation patients from publicly available data [33], of which 600 cases were used for training and the remaining 150 cases for testing.

Table 1: Data splitting (in number of samples) for anomaly detection and localization

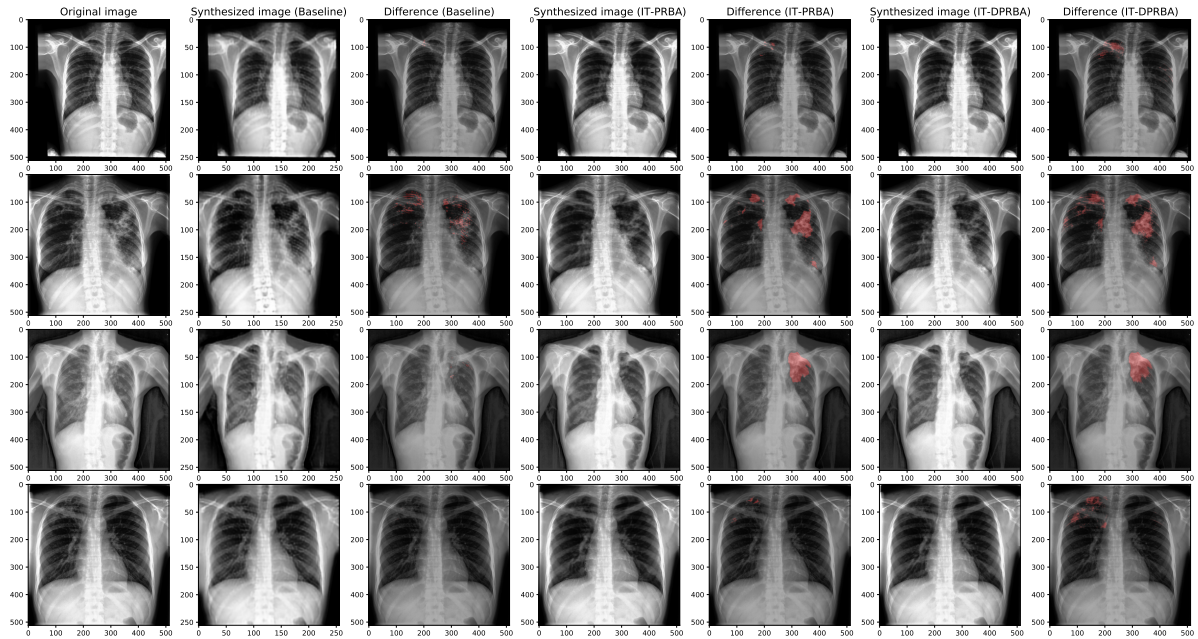
Case	Normal	Tuberculosis	Consolidation
Training set	600	600	600
Test set	758	150	150

4.2 Lung segmentation for data preprocessing

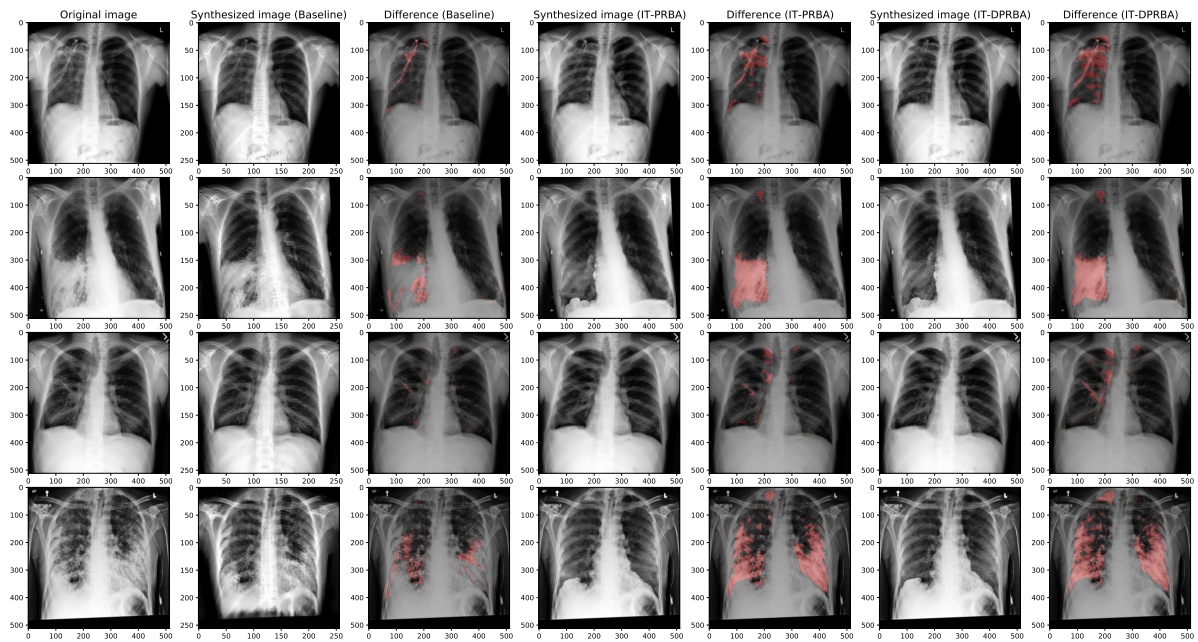
We segmented lung regions from each CXR image using a publicly available pretrained lung segmentation network [34] based on a variational autoencoder, which achieves a higher generalization performance than other networks. We used the JSRT [35] and NLM [36] datasets to evaluate the lung segmentation performance of the pretrained network in terms of the intersection over union

Table 2: Segmentation performance in terms of IOU and Dice coefficient of method in [34]

	Dataset	IOU	Dice
Method in [34]	JSRT [35]	0.939	0.969
	NLM [36]	0.942	0.970



(a)



(b)

Figure 6: Comparison between AL-CXR maps v_t obtained from proposed method and baseline for (a) tuberculosis and (b) consolidation patients. All were commonly used based on CUT.

(IOU) and Dice coefficient between the actual region of the lung in a 2D image and its prediction, as listed in Table 2. In both datasets, the values are at least 0.93, confirming a high segmentation performance. Various segmentation results are shown in supplementary Fig. S1.

Table 3: AUC of GAN-IT models (CycleGAN and CUT) for patient-wise anomaly score $\|\mathcal{H}(v_t, \tau)\|_2$ in tuberculosis cases. The receiver operating characteristic curve is presented in supplementary Fig. S2.

	CUT			CycleGAN		
	$\tau = 20$	$\tau = 30$	$\tau = 40$	$\tau = 20$	$\tau = 30$	$\tau = 40$
Baseline	0.823	0.755	0.691	0.678	0.624	0.586
IT-PRBA (Ours)	0.904	0.910	0.891	0.890	0.886	0.879
IT-DPRBA (Ours)	0.915	0.928*	0.919	0.890	0.891	0.881

Table 4: AUC of GAN-IT models (CycleGAN and CUT) for patient-wise anomaly score $\|\mathcal{H}(v_t, \tau)\|_2$ in consolidation cases. The receiver operating characteristic curve is shown in supplementary Fig. S2.

	CUT			CycleGAN		
	$\tau = 20$	$\tau = 30$	$\tau = 40$	$\tau = 20$	$\tau = 30$	$\tau = 40$
Baseline	0.971	0.964	0.952	0.870	0.847	0.830
IT-PRBA (Ours)	0.975	0.986	0.984	0.975	0.970	0.960
IT-DPRBA (Ours)	0.982	0.991*	0.990	0.968	0.973	0.968

4.3 Results for anomaly detection

4.3.1 Evaluation Metric: Patient-wise Anomaly Score

We evaluated AL-CXR using difference v_t in pixel values between the reconstructed and original images given by (2). In addition, we calculated the patient-wise anomaly score to obtain a confidence level for whether the target CXR image contains an anomaly. This score was calculated as the ℓ_2 -norm, $\|\mathcal{H}(v_t, \tau)\|_2$, of anomaly map v_t , which was obtained by thresholding, via $\mathcal{H}(v_t, \tau)$, the absolute value of v_t , with a value below $\tau \in (20, 30, 40)$ being set to 0 at the pixel level as follows:

$$\mathcal{H}_{xy}(v_t, \tau) = \begin{cases} v_t(x, y), & \text{if } |v_t(x, y)| > \tau \text{ for } (x, y) \in \text{supp}(v_t), \\ 0, & \text{for all } (x, y) \notin \text{supp}(v_t). \end{cases}$$

To measure the discrimination ability between normal and abnormal cases, we calculated the region under the receiver operating characteristic curve (AUC) of patient-wise anomaly score $\|\mathcal{H}(v_t, \tau)\|_2$.

4.3.2 Performance comparison

By integrating the proposed IT-PRBA or IT-DPRBA, we trained GAN-IT to evaluate anomaly detection and localization. Anomaly localization was performed on the pretrained GAN-IT model described by (1) using training data from normal (Y) and abnormal (X) cases for tuberculosis or consolidation. The results were compared with those of a baseline using an existing GAN-IT without registration and deregistration, as shown in Fig. 4. For a fair comparison, we applied the GAN-IT CycleGAN [7] or CUT [8] to the proposed and baseline methods. For abnormal data, either tuberculosis or consolidation cases were used.

Additional details on the training setup of GAN-IT are given as follows: in all the experiments, we adjusted the image size to 256×256 pixels, set the minibatch size to 24 and the number of epochs to 150, and used the Adam optimizer with an initial learning rate of $4 \cdot 10^{-5}$. To optimize performance, the learning rate was linearly decreased until reaching 0 at the last epoch. We collected CXR unpaired training data corresponding to the input and output of the model to train the GAN-IT model and provided the CXR image of a normal patient by receiving an abnormal CXR image with a specific disease (e.g., tuberculosis [32] and consolidation [33]) as an input.

The anomaly detection performance for tuberculosis and consolidation is listed in Tables 3 and 4, respectively. The AUC of the CUT model is higher than that of CycleGAN in all the cases. For CUT, compared with the existing baseline GAN-IT without IT-PRBA or IT-DPRBA (Fig. 4), the proposed IT-PRBA or IT-DPRBA improves the AL-CXR AUCs at various τ values by more than 4%. Among the proposed methods, IT-DPRBA outperforms IT-PRBA in most cases (values in boldface). The values showing the highest performance (marked with *) were obtained from IT-DPRBA. These results validate the proposed IT-PRBA and its DL-based extension, IT-DPRBA.

Table 5: Anomaly detection performance for tuberculosis cases according to whether the proposed DLF-PR and/or BA are applied. B, baseline; R, registration; A, data augmentation; B+R+A, proposed IT-PRBA

	CUT			CycleGAN		
	$\tau = 20$	$\tau = 30$	$\tau = 40$	$\tau = 20$	$\tau = 30$	$\tau = 40$
B	0.823	0.755	0.691	0.678	0.624	0.586
B+R	0.861	0.884	0.888	0.886	0.878	0.863
B+R+A (Ours)	0.904	0.910	0.891	0.890	0.886	0.879

Table 6: Anomaly detection performance for consolidation cases according to whether the proposed DLF-PR and/or BA are applied. B, baseline; R, registration; A, data augmentation; B+R+A, proposed IT-PRBA

	CUT			CycleGAN		
	$\tau = 20$	$\tau = 30$	$\tau = 40$	$\tau = 20$	$\tau = 30$	$\tau = 40$
B	0.971	0.964	0.952	0.870	0.847	0.830
B+R	0.955	0.970	0.970	0.975	0.969	0.959
B+R+A (Ours)	0.975	0.986	0.984	0.975	0.970	0.960

Fig. 6 shows AL-CXR examples using CUT from localization maps v_t given by (2) for tuberculosis or consolidation cases. For simplicity, negative values of v_t are treated as 0. The proposed IT-PRBA and IT-DPRBA detect abnormal regions in the lung images that are not detected by the baselines. Examples using CycleGAN for abnormal cases and CycleGAN/CUT for normal cases are shown in supplementary Figs. S3 and S4.

4.3.3 Ablation study for registration and data augmentation in IT-PRBA

The proposed IT-PRBA applies DLF-PR and BA to an existing GAN-IT baseline. We conducted an ablation study to confirm whether DLF-PR and BA contribute to CXR anomaly detection, and the results are listed in Tables 5 and 6 for tuberculosis and consolidation cases, respectively. These results show that when registration and data augmentation are sequentially added to the baseline, the anomaly detection performance improves, validating IT-PRBA and its components.

4.4 Results for anomaly localization

We utilized the public dataset [32] to demonstrate that the proposed method (i.e., IT-DPRBA and IT-PRBA) provides superior performance for anomaly localization compared to the existing method. Because of the fact that this data set includes tuberculosis location information as a bounding box, model performance can be evaluated by measuring the correlation between the tuberculosis location output by the model and this bounding box.

4.4.1 Evaluation metric: Patient-wise anomaly score

In other words, model performance can be compared by quantifying the proportion of anomaly regions predicted by the proposed model that fall within this bounding box relative to other models. To show this, we represent $z_t = v_t \odot g_t$ as the intersection area between the anomaly map v_t predicted by the model for the t -th patient and the bounding box g_t , where $g_t \in \{0, 1\}^2$ denotes the ground truth binary mask for the tuberculosis location bounding box of the t -th tuberculosis patient such that the $v_t(x, y)$ value of the pixel location (x, y) in tuberculosis is 1 and otherwise 0. Then from the intersection area z_t of t -th patient, we can derive the following two performance evaluation metrics, $s_{intensity}$ and s_{binary} in (15), for the anomaly localization:

$$\begin{aligned}
 s_{intensity}(t) &:= \sum_{xy} \mathcal{H}_{xy}(z_t, \tau), \\
 s_{binary}(t) &:= \sum_{xy} \mathcal{P}_{xy}(z_t, \tau),
 \end{aligned} \tag{15}$$

Table 7: Comparison of performance between techniques of anomaly localization in terms of $s_{intensity}$; proposed IT-DPRBA, IT-PRBA, and baseline method ($\tau : 25, 30, 35$ and the score was divided by 10^3)

	CUT			CycleGAN		
	$\tau = 25$	$\tau = 30$	$\tau = 35$	$\tau = 25$	$\tau = 30$	$\tau = 35$
Baseline	4.450	2.976	1.859	1.066	0.437	0.156
IT-PRBA (Ours)	4.984	3.641	2.610	4.370	3.334	2.517
IT-DPRBA (Ours)	5.822	4.387	3.241	6.361*	4.965	3.821

where

$$\mathcal{P}(z_t, \tau) = \begin{cases} 1, & \text{if } z_t(x, y) \geq \tau \text{ for } (x, y) \in \text{supp}(z_t), \\ 0, & \text{for all } (x, y) \notin \text{supp}(z_t). \end{cases} \quad (16)$$

Here, $\mathcal{H}(z_t, \tau)$ (defined in (15)) and $\mathcal{P}_{xy}(z_t, \tau)$ (defined in (16)) refer to the operations delivering the target pixel-wise anomaly score $z_t(x, y)$ at location (x, y) as-is or binarizing it respectively if its original score $z_t(x, y)$ predicted by the model in the bounding box is greater than a specific threshold. After this operation, we merged the anomaly score value for each pixel inside the bounding box so obtain the final anomaly localization scores $s_{intensity}(t)$ and $s_{binary}(t)$ for each patient (i.e., t -th patient).

4.4.2 Performance comparison for AL-CXR

For these two scores $s_{intensity}$ and s_{binary} , we calculated and displayed their mean for a total of N (i.e., 150) patients in Tables 7 and 8, respectively. As a result, it was demonstrated for representative GAN-IT backbone networks (CycleGAN or CUT) and various thresholds τ that the proposed method (i.e., IT-DPRBA and IT-PRBA) has a consistent performance improvement of AL-CXR compared to the existing baseline method (i.e., an existing GAN-IT without our registration and deregistration). In particular, in the case of the best performance (as marked with * in each of tables), the proposed IT-DPRBA significantly improved the performance of anomaly localization more than 6 times compared to the baseline. Further, in the comparison between the proposed methods, IT-DPRBA showed a consistent performance improvement compared to IT-PRBA, thereby proving the validity of both proposed methods on AL-CXR. In Figs. 6 and S3, the same trend of performance improvement for anomaly localization (i.e., Baseline < IT-PRBA < IT-DPRBA) can also be observed.

4.5 Results for deformable registration

We compared the proposed registration techniques, namely, DLF-PR and DL-PR, with the existing gold standard DL methods (i.e., Baselines A and B as shown in Section 3.5). Accordingly, coordinate transformation functions (from moving to fixed) were individually obtained from DLF-PR using $T_{i \rightarrow f}^l$ in (4) and $T_{i \rightarrow f}^r$ in (6), DL-PR using $REG_{\phi_{i \rightarrow f}^{l*}}$ and $REG_{\phi_{i \rightarrow f}^{r*}}$, and DL-based registration baselines A using $REG_{\psi_{i \rightarrow f}^{l*}}$ and $REG_{\psi_{i \rightarrow f}^{r*}}$ and B using $REG_{\pi_{i \rightarrow f}^{l*}}$ and $REG_{\pi_{i \rightarrow f}^{r*}}$, together with each of their inverse maps.

We used U-Net [37, 38] as the backbone for DL-based registration because it achieves state-of-the-art performance [5]. For training, we used mean squared error $\mathcal{L}_\phi(a, b)$ as the loss function and the Adam optimizer [39] with a learning rate of 0.0001. The number of epochs was set to 1000, and the batch size was set to 1.

Fig. 7 shows the registration/moved results from the moving images to the fixed images. Unlike other methods, the proposed DL-PR fully registers images without artifacts (no yellow or red box). Relatively

Table 8: Comparison of performance between techniques of anomaly localization in terms of s_{binary} ; proposed IT-DPRBA, IT-PRBA, and baseline method ($\tau : 25, 30, 35$ and the score was divided by 10^3)

	CUT			CycleGAN		
	$\tau = 25$	$\tau = 30$	$\tau = 35$	$\tau = 25$	$\tau = 30$	$\tau = 35$
Baseline	156.4	116.7	81.1	33.2	16.4	7.5
IT-PRBA (Ours)	194.8	158.0	124.6	180.8	152.4	125.9
IT-DPRBA (Ours)	230.8	192.1	155.6	268.0*	230.5	193.9

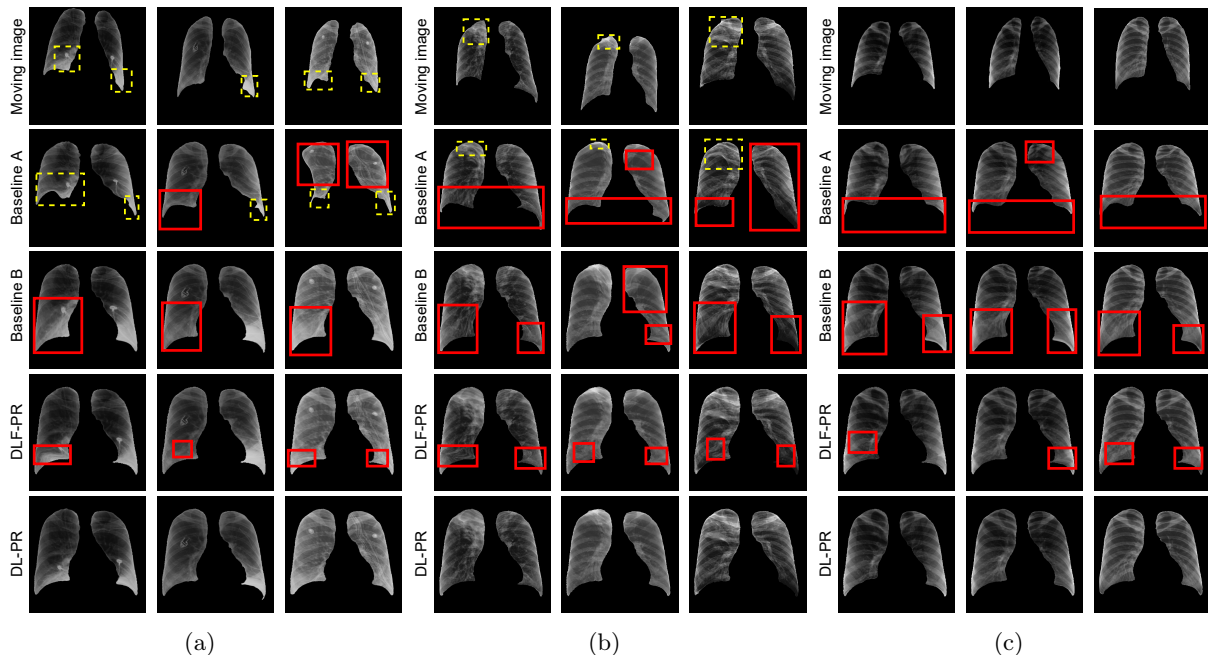


Figure 7: Performance of registration techniques for (a) consolidation, (b) tuberculosis, and (c) normal cases. Registered/moved CXR images were individually given by proposed DL-PR/DLF-PR and baselines A/B. Our registration technique provides fewer or no artifacts (Our DL-PR has no disease distortion and reduction (as shown in the yellow box) and artificial shading or insufficient conversion by lung imbalance transformation (as shown in the red box)). Additional images are shown in supplementary Figs. S6, S7, and S8

few artifacts are observed in DLF-PR compared with the two existing DL-based baselines. As DLF-PR is not based on DL, it does not require training and provides fast registration. DL-PR does not generate artifacts compared with other methods. Therefore, the proposed DLF-PR and DL-PR are effective and achieve high performance.

5 Conclusion

Despite the fact that unpaired image translation demonstrates a high potential for quantifying lung disease without pixel annotation, its practical application is limited due to the a fundamental issue of performance degradation caused by the inconsistency of data for image translation learning. In other words, the underlying cause cause of this problem is that the heterogeneity between the reference lung for registration and the moving lung target results in unavoidable artifacts when the image coordinates are converted into one standard region even using the current state-of-the-art DL-based deformable registration techniques. To address this fundamental challenge, we developed a registration technique that employs both linear and (DL-based) non-linear coordinate transformations, enabling consistent and natural movement throughout the lung region. Though this advanced nature, our registration can be applied for the first time as a means for the input and output of an image translation network to result in a single reference domain, whereas previous image translation studies did not apply the registration technique that can unify all images with this single reference domain. In addition, we presented a new data augmentation methodology suitable for this standard domain and applied it in conjunction with the

proposed registration to increase the performance of CXR anomaly localization/quantification via image translation in comparison to the prior baselines. Although we only validated our registration-based image translation model on CXR images, its principle can be extended to other applications. Accordingly, we expect our method will serve as a baseline for anomaly localization even without pixel-level annotations of diseases that can be detected using various medical imaging modalities.

Appendix: Supplementary Materials

Implementation details for REG and BA

In this section, we detail the implementation of the proposed REG and BA, which are used in Algorithm 1, as Algorithms 4 and 5, respectively.

Algorithm 4 REG

$T_{i \rightarrow f}^u, T_{f \rightarrow i}^u \leftarrow \text{REG}(s_i^u, s_f^u) \quad (u \in \{l, r\}) :$

Input: (s_i, s_f) for some $i \in \{1 : n\}$

- 1: $(x_f^{low}, y_f^{low}) \leftarrow$ find (x, y) -coordinate s.t. y is given as the smallest in boundary set of s_f^u .
- 2: $(x_i^{low}, y_i^{low}) \leftarrow$ find (x, y) -coordinate s.t. y is given as the smallest in boundary set of s_i^u .
- 3: $(x_f^{high}, y_f^{high}) \leftarrow$ find (x, y) -coordinate s.t. its l_2 -distance to (x_f^{low}, y_f^{low}) is given as the largest in boundary set of s_f^u .
- 4: $(x_i^{high}, y_i^{high}) \leftarrow$ find (x, y) -coordinate s.t. its l_2 -distance to (x_i^{low}, y_i^{low}) is given as the largest in boundary set of s_i^u .
- 5: $\mathcal{R}_f \leftarrow$ obtain coordinate rotation function \mathcal{R}_f to rotate image s_f^u as $\mathcal{R}_f(s_f^u)$ s.t. rotated x_f^{low} and rotated x_f^{high} are equal
- 6: $\mathcal{R}_i \leftarrow$ obtain coordinate rotation function \mathcal{R}_i to rotate image s_i^u as $\mathcal{R}_i(s_i^u)$ s.t. rotated x_i^{low} and rotated x_i^{high} are equal
- 7: $\mathcal{V}_i \leftarrow$ obtain coordinate resizing function \mathcal{V}_i s.t. the longest vertical lengths of positive regions in $\mathcal{V}_i(\mathcal{R}_i(s_i^u))$ and $\mathcal{R}_f(s_f^u)$ are equal and the corresponding columns are on the same y -axis coordinates
- 8: $\mathcal{H}_i \leftarrow$ obtain coordinate resizing function \mathcal{H}_i s.t. for each y -axis coordinate, the horizontal lengths of positive regions in $\mathcal{H}_i(\mathcal{V}_i(\mathcal{R}_i(s_i^u)))$ and $\mathcal{R}_f(s_f^u)$ are equal
- 9: $T_{i \rightarrow f}^u(\cdot) \leftarrow$ obtain the final coordinate transform as $\mathcal{R}_f^{-1}(\mathcal{H}_i(\mathcal{V}_i(\mathcal{R}_i(\cdot))))$, where $\mathcal{R}_f^{-1}(\cdot)$ denotes the inverse map of $\mathcal{R}_f(\cdot)$
- 10: $T_{f \rightarrow i}^u(\cdot) \leftarrow$ obtain an inverse coordinate transform map of $T_{i \rightarrow f}^u(\cdot)$ s.t. $T_{f \rightarrow i}^u(T_{i \rightarrow f}^u(\cdot)) = \mathcal{I}(\cdot)$

Output: $T_{i \rightarrow f}^u, T_{f \rightarrow i}^u$

Algorithm 5 BA

$\hat{x}_{i \rightarrow f}^l \leftarrow \text{BA}_{r \rightarrow l}(x_{i \rightarrow f}^r, s_f^l) :$

Input: $(x_{i \rightarrow f}^r, s_f^l)$ for some $i \in \{1 : n\}$

- 1: $h_{i \rightarrow f}^l \leftarrow$ flip $\mathcal{R}_f(x_{i \rightarrow f}^r)$ horizontally
- 2: $h_{i \rightarrow f}^l \leftarrow$ resize vertically $h_{i \rightarrow f}^l$ for its longest vertical line to match that of $\mathcal{R}_f(s_f^l)$
- 3: $h_{i \rightarrow f}^l \leftarrow$ resize the horizontal length of $h_{i \rightarrow f}^l$ to match that of $\mathcal{R}_f(s_f^l)$ at each y -axis coordinate
- 4: $\mathcal{R}_f^{-1}(\cdot) \leftarrow$ obtain inverse map of $\mathcal{R}_f(\cdot)$ s.t. $\mathcal{R}_f^{-1}(\mathcal{R}_f(s_f^l)) = s_f^l$

Output: $\hat{x}_{i \rightarrow f}^l = \mathcal{R}_f^{-1}(h_{i \rightarrow f}^l)$

$\hat{x}_{i \rightarrow f}^r \leftarrow \text{BA}_{l \rightarrow r}(x_{i \rightarrow f}^l, s_f^r) :$

Input: $(x_{i \rightarrow f}^l, s_f^r)$ for some $i \in \{1 : n\}$

- 1: $h_{i \rightarrow f}^r \leftarrow$ flip $\mathcal{R}_f(x_{i \rightarrow f}^l)$ horizontally
- 2: $h_{i \rightarrow f}^r \leftarrow$ resize vertically $h_{i \rightarrow f}^r$ for its longest vertical line to match that of $\mathcal{R}_f(s_f^r)$
- 3: $h_{i \rightarrow f}^r \leftarrow$ remove right-sided/horizontal part of positive regions in $h_{i \rightarrow f}^r$ for remaining part to match that of positive regions in $\mathcal{R}_f(s_f^r)$ at each y -axis coordinate if horizontal length l_a of positive regions in $h_{i \rightarrow f}^r$ is larger than l_b of positive regions in $\mathcal{R}_f(s_f^r)$ (i.e., $l_a \geq l_b$). Otherwise, resize it for its length to match l_b
- 4: $\mathcal{R}_f^{-1}(\cdot) \leftarrow$ obtain inverse map of $\mathcal{R}_f(\cdot)$ s.t. $\mathcal{R}_f^{-1}(\mathcal{R}_f(s_f^r)) = s_f^r$

Output: $\hat{x}_{i \rightarrow f}^r = \mathcal{R}_f^{-1}(h_{i \rightarrow f}^r)$

Registration REG in Algorithm 4 provides coordinate shift functions $T_{i \rightarrow f}^l$ and $T_{i \rightarrow f}^r$ mapping from left

s_i^l and right s_i^r of the lung mask of patient i to s_f^l and s_f^r of a given fixed lung mask s_f , respectively, where i and f denote the patient index (for moving images) and fixed image, respectively. Steps 1–4 calculate the longest vertical line (e.g., yellow vertical line in Fig. 3(b)) starting from the lowest point (steps 1 and 2) on the outer edge of each left or right lung mask. Steps 5 and 6 calculate coordinate rotation functions \mathcal{R}_i and \mathcal{R}_f , which rotate moving mask s_i^u and fixed mask s_f^u , respectively, thus satisfying their longest lines perpendicular to the horizontal axis and calculated in the previous steps. Step 7 calculates vertical coordinate resizing function \mathcal{V}_i for the longest vertical line of the lung in moving $\mathcal{R}_i(s_i^u)$ to match that in fixed $\mathcal{R}_f(s_f^u)$. Step 8 derives horizontal coordinate resizing function \mathcal{H}_i for each horizontal length of the lung image while moving $\mathcal{V}_i(\mathcal{R}_i(s_i^u))$ to match that in fixed $\mathcal{R}_f(s_f^u)$. Finally, step 9 calculates the coordinate transform map as $T_{i \rightarrow f}^u(\cdot) = \mathcal{R}_f^{-1}(\mathcal{H}_i(\mathcal{V}_i(\mathcal{R}_i(\cdot))))$. This includes returning the registered image $\mathcal{H}_i(\mathcal{V}_i(\mathcal{R}_i(s_i^u)))$ to the original axis of rotation.

The proposed data augmentation algorithms, $\text{BA}_{r \rightarrow l}$ and $\text{BA}_{l \rightarrow r}$, in Algorithm 5 generate additional data by transforming the right ($x_{i \rightarrow f}^r$) and left ($x_{i \rightarrow f}^l$) lung images into left ($\hat{x}_{i \rightarrow f}^l$) and right ($\hat{x}_{i \rightarrow f}^r$) lung images, respectively. Because the right lung image has a horizontally narrower lung region owing to the presence of the heart, after flipping the left image to the right (steps 1 and 2 in $\text{BA}_{r \rightarrow l}$), we partially remove the inner region of the flipped image considering a synthetic heart region to fit the original right lung, as shown in step 3 of $\text{BA}_{r \rightarrow l}$.

Supplementary figures

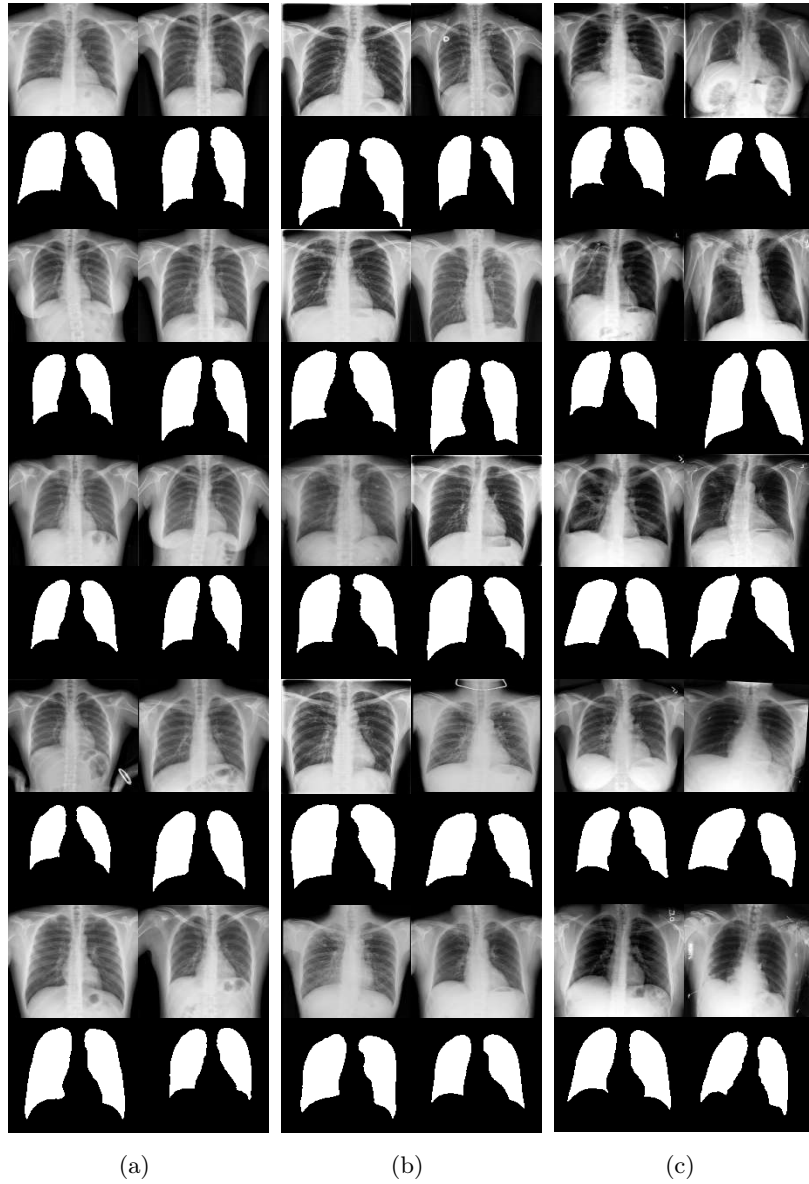


Figure S1: Examples of lung masks predicted by the segmentation network for (a) normal, (b) tuberculosis, and (c) consolidation cases.

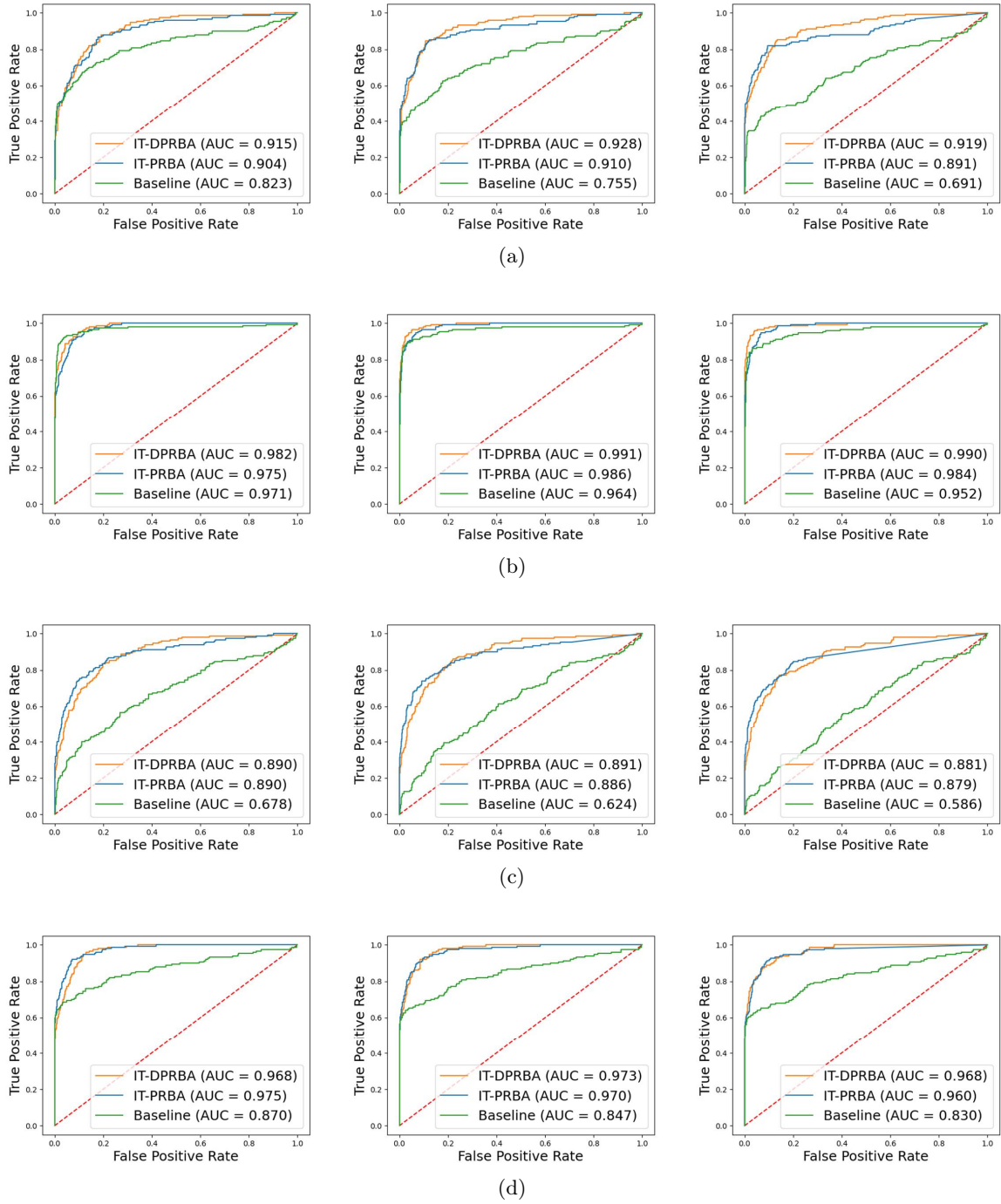
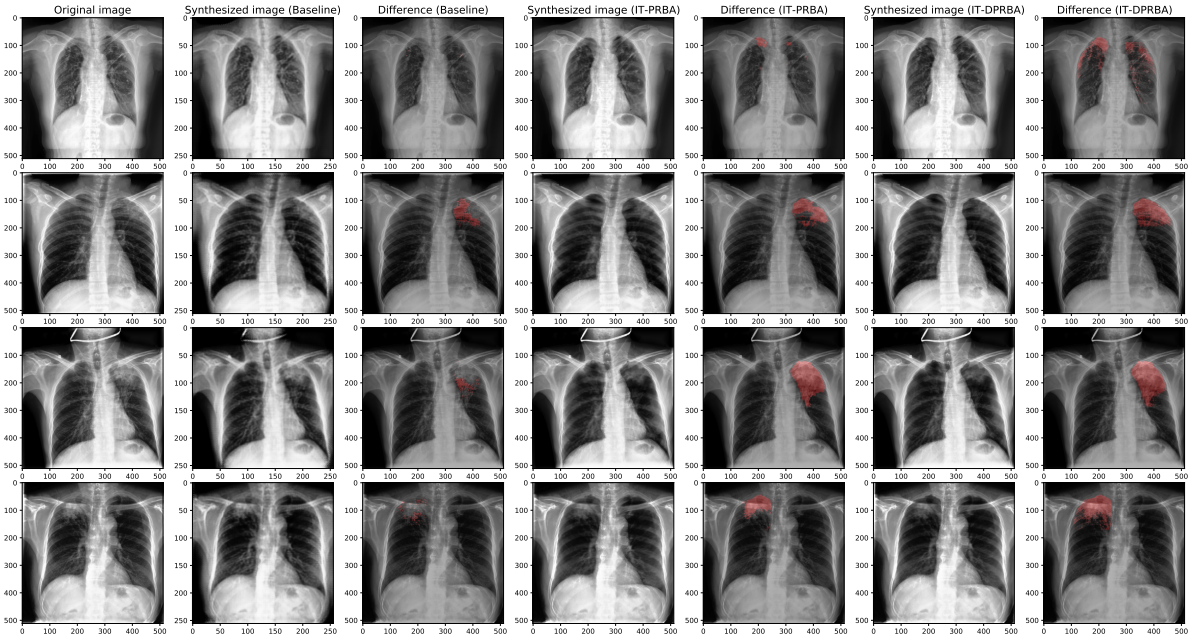
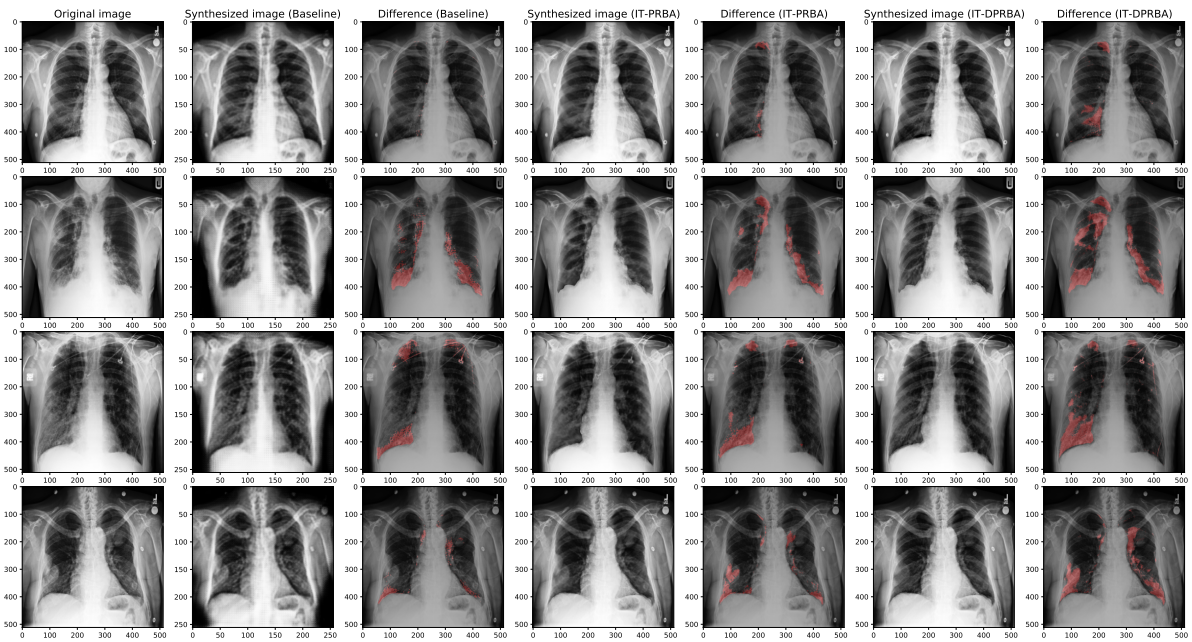


Figure S2: Performance comparison of AL-CXR in terms of AUC with varying threshold $\tau = (20, 30, 40)$ (from left to right). Proposed method compared with CUT baseline for (a) tuberculosis and (b) consolidation cases. Proposed method compared with CycleGAN baseline for (c) tuberculosis and (d) consolidation cases.

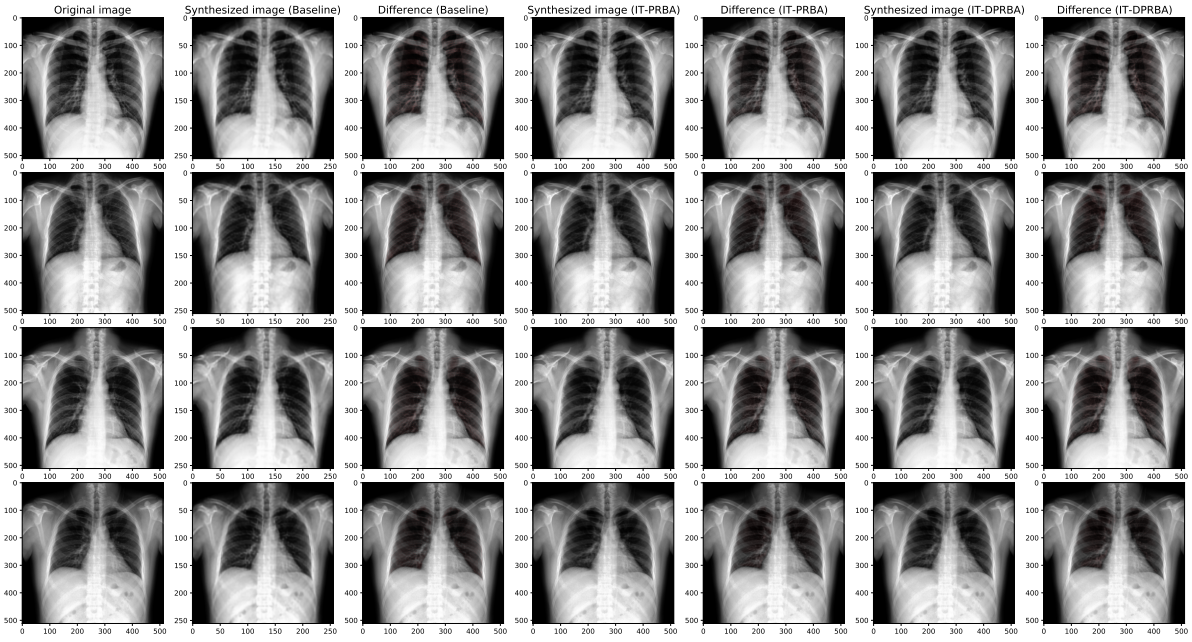


(a)

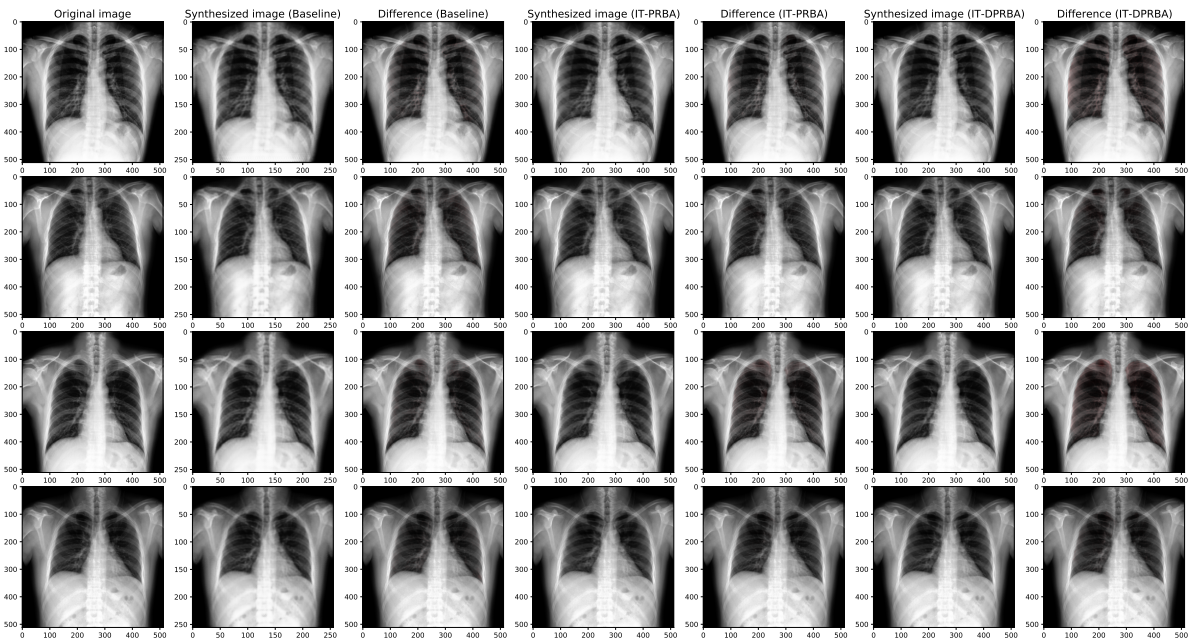


(b)

Figure S3: Comparison between anomaly localization maps v_t obtained from proposed method and baseline for (a) tuberculosis and (b) consolidation cases. All were commonly used based on CycleGAN.



(a)



(b)

Figure S4: Comparison between anomaly localization maps v_t obtained from proposed method and baseline for normal patients. All were commonly used based on (a) CUT or (b) CycleGAN.

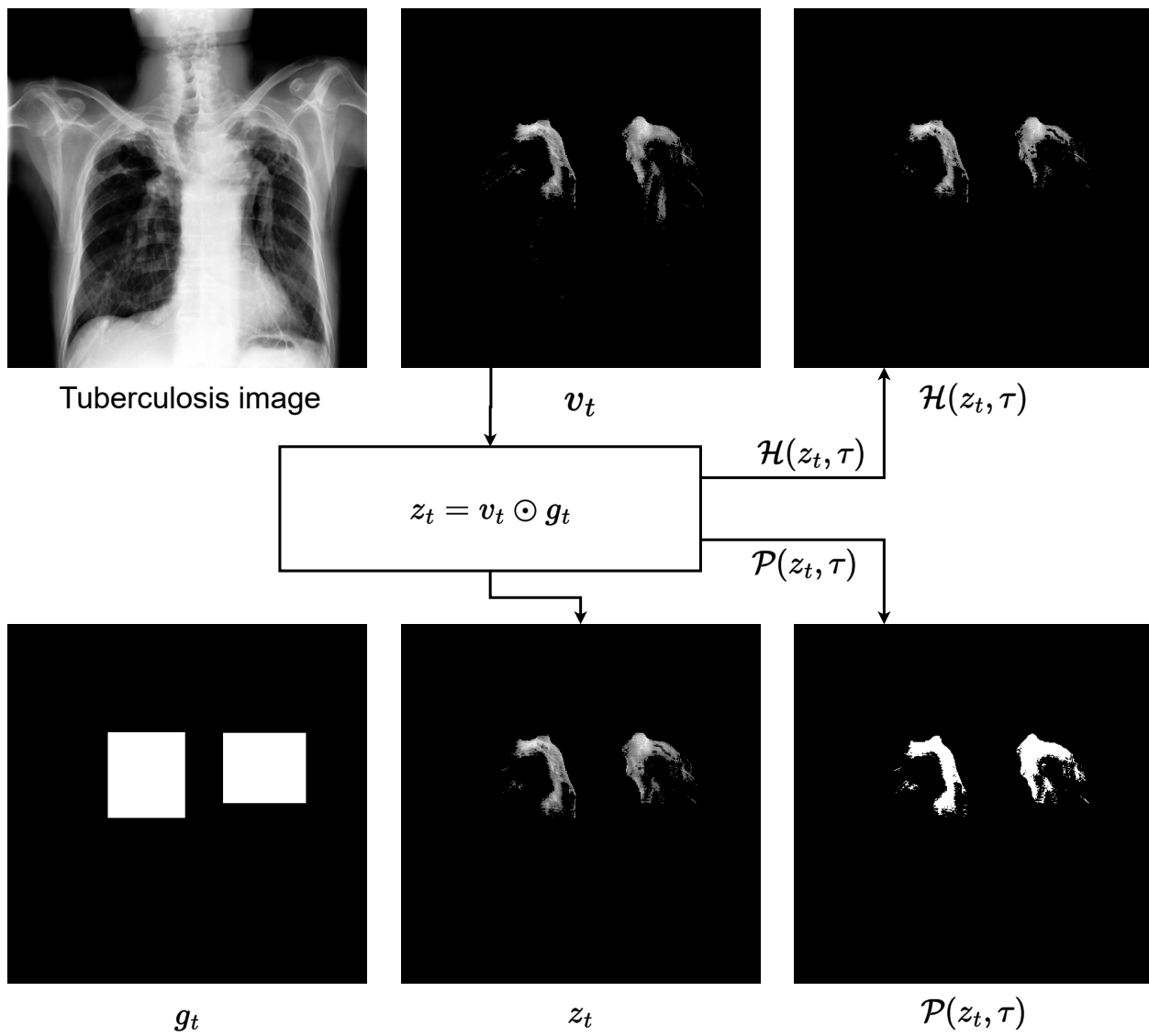


Figure S5: Illustration of how to derive metrics to compare and evaluate the performance of AI techniques for lung anomaly localization

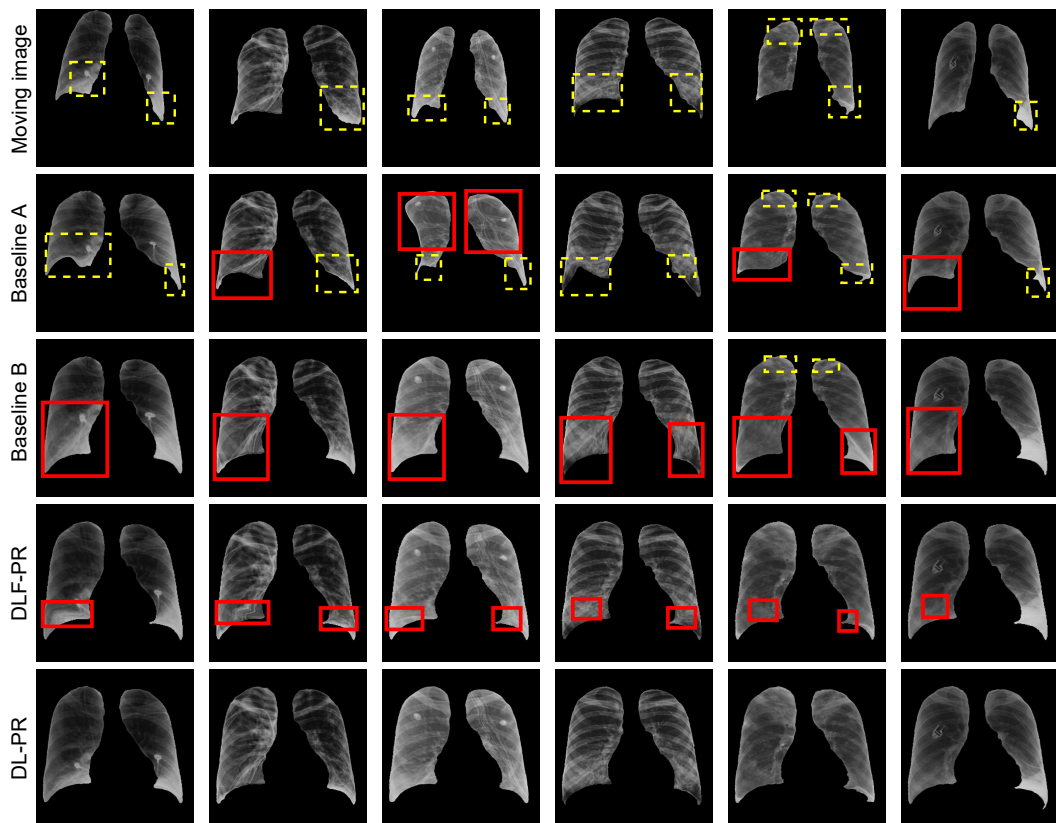


Figure S6: Performance comparison between registration techniques for consolidation case. The registered/moved CXR images were obtained from the proposed DL-PR/DLF-PR and baselines A/B. Our registration approach has fewer or no artifacts.

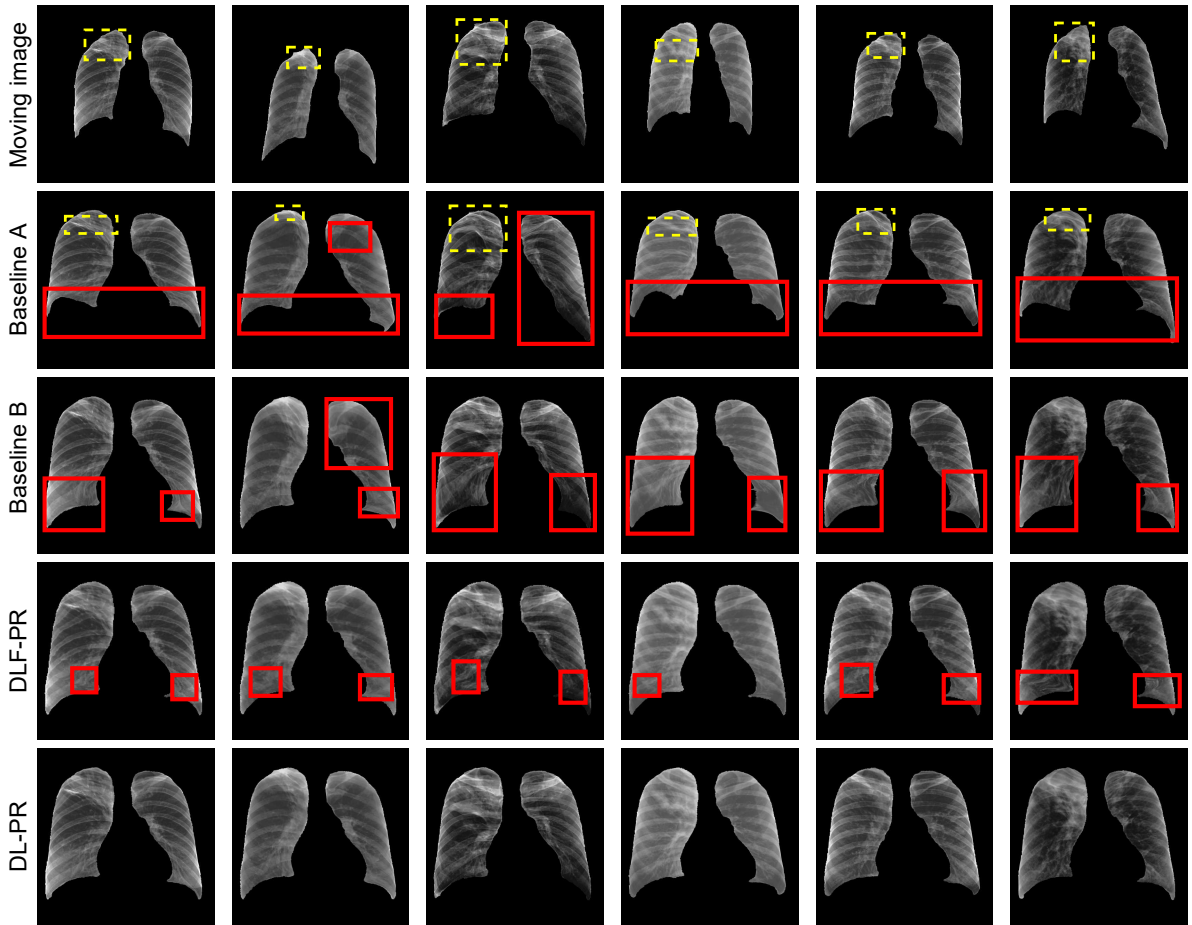


Figure S7: Performance comparison between registration techniques for tuberculosis case. The registered/moved CXR images were obtained from the proposed DL-PR/DLF-PR and baselines A/B. Our registration approach has fewer or no artifacts.

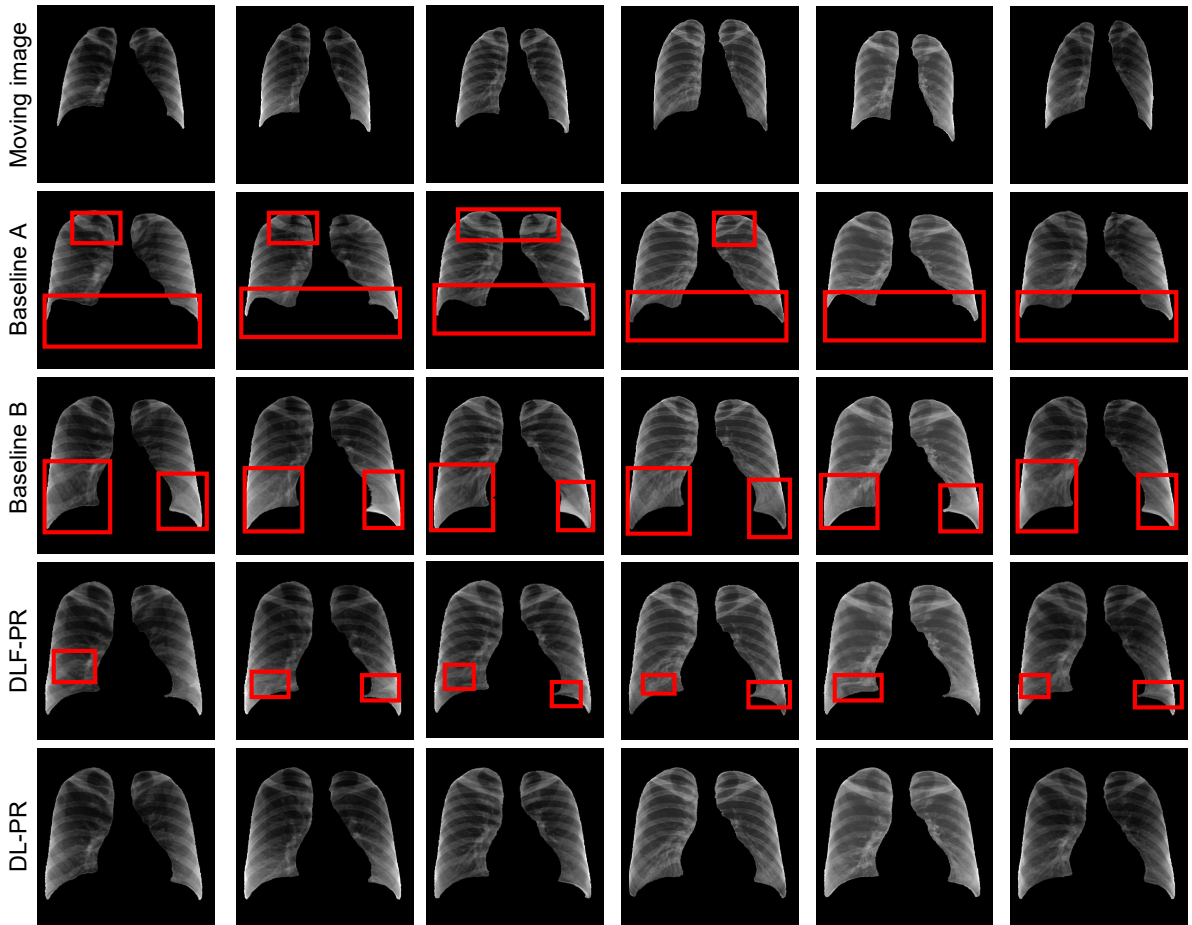


Figure S8: Performance comparison between registration techniques for normal case. The registered/moved CXR images were obtained from the proposed DL-PR/DLF-PR and baselines A/B. Our registration approach has fewer or no artifacts.

References

- [1] Wesley H Self, D Mark Courtney, Candace D McNaughton, Richard G Wunderink, and Jeffrey A Kline. High discordance of chest X-ray and computed tomography for detection of pulmonary opacities in ED patients: Implications for diagnosing pneumonia. *The American Journal of Emergency Medicine*, 31(2):401–405, 2013.
- [2] Rachna Jain, Meenu Gupta, Soham Taneja, and D Jude Hemanth. Deep learning based detection and analysis of COVID-19 on chest X-ray images. *Applied Intelligence*, 51(3):1690–1700, 2021.
- [3] Soumya Ranjan Nayak, Deepak Ranjan Nayak, Utkarsh Sinha, Vaibhav Arora, and Ram Bilas Pachori. Application of deep learning techniques for detection of COVID-19 cases using chest X-ray images: A comprehensive study. *Biomedical Signal Processing and Control*, 64:102365, 2021.
- [4] Karim Hammoudi, Halim Benhabiles, Mahmoud Melkemi, Fadi Dornaika, Ignacio Arganda-Carreras, Dominique Collard, and Arnaud Scherpereel. Deep learning on chest X-ray images to detect and evaluate pneumonia cases at the era of COVID-19. *Journal of Medical Systems*, 45(7):1–10, 2021.
- [5] Guha Balakrishnan, Amy Zhao, Mert R Sabuncu, John Guttag, and Adrian V Dalca. Voxelmorph: A learning framework for deformable medical image registration. *IEEE Transactions on Medical Imaging*, 38(8):1788–1800, 2019.
- [6] Malte Hoffmann, Benjamin Billot, Douglas N Greve, Juan Eugenio Iglesias, Bruce Fischl, and Adrian V Dalca. SynthMorph: Learning contrast-invariant registration without acquired images. *IEEE Transactions on Medical Imaging*, 41(3):543–558, 2021.
- [7] Jun-Yan Zhu, Taesung Park, Phillip Isola, and Alexei A Efros. Unpaired image-to-image translation using cycle-consistent adversarial networks. In *Proceedings of the IEEE International Conference on Computer Vision*, pages 2223–2232, 2017.
- [8] Taesung Park, Alexei A Efros, Richard Zhang, and Jun-Yan Zhu. Contrastive learning for unpaired image-to-image translation. In *European Conference on Computer Vision*, pages 319–345. Springer, 2020.
- [9] Thomas Schlegl, Philipp Seeböck, Sebastian M Waldstein, Ursula Schmidt-Erfurth, and Georg Langs. Unsupervised anomaly detection with generative adversarial networks to guide marker discovery. In *International Conference on Information Processing in Medical Imaging*, pages 146–157. Springer, 2017.
- [10] Thomas Schlegl, Philipp Seeböck, Sebastian M Waldstein, Georg Langs, and Ursula Schmidt-Erfurth. f-AnoGAN: Fast unsupervised anomaly detection with generative adversarial networks. *Medical Image Analysis*, 54:30–44, 2019.
- [11] Panpan Zheng, Shuhan Yuan, Xintao Wu, Jun Li, and Aidong Lu. One-class adversarial nets for fraud detection. In *Proceedings of the AAAI Conference on Artificial Intelligence*, volume 33, pages 1286–1293, 2019.
- [12] Phuc Cuong Ngo, Amadeus Aristo Winarto, Connie Khor Li Kou, Sojeong Park, Farhan Akram, and Hwee Kuan Lee. Fence GAN: Towards better anomaly detection. In *2019 IEEE 31st International Conference on Tools with Artificial Intelligence*, pages 141–148. IEEE, 2019.

- [13] Pramuditha Perera, Ramesh Nallapati, and Bing Xiang. OCGAN: One-class novelty detection using GANs with constrained latent representations. In *Proceedings of the IEEE/CVF Conference on Computer Vision and Pattern Recognition*, pages 2898–2906, 2019.
- [14] Nitish Bhatt, David Ramon Prados, Nedim Hodzic, Christos Karanassios, and HR Tizhoosh. Unsupervised detection of lung nodules in chest radiography using generative adversarial networks. *arXiv preprint:2108.02233*, 2021.
- [15] Yu-Xing Tang, You-Bao Tang, Mei Han, Jing Xiao, and Ronald M Summers. Abnormal chest X-ray identification with generative adversarial one-class classifier. In *IEEE 16th International Symposium on Biomedical Imaging*, pages 1358–1361. IEEE, 2019.
- [16] Yu-Xing Tang, You-Bao Tang, Mei Han, Jing Xiao, and Ronald M Summers. Deep adversarial one-class learning for normal and abnormal chest radiograph classification. In *Medical Imaging 2019: Computer-Aided Diagnosis*, volume 10950, page 1095018. International Society for Optics and Photonics, 2019.
- [17] Muhammad Zaigham Zaheer, Jin-ha Lee, Marcella Astrid, and Seung-Ik Lee. Old is gold: Redefining the adversarially learned one-class classifier training paradigm. In *Proceedings of the IEEE/CVF Conference on Computer Vision and Pattern Recognition*, pages 14183–14193, 2020.
- [18] Krishna Nand Keshavamurthy, Carsten Eickhoff, and Krishna Juluru. Weakly supervised pneumonia localization in chest X-rays using generative adversarial networks. *Medical Physics*, 2021.
- [19] Youbao Tang, Yuxing Tang, Yingying Zhu, Jing Xiao, and Ronald M Summers. A disentangled generative model for disease decomposition in chest X-rays via normal image synthesis. *Medical Image Analysis*, 67:101839, 2021.
- [20] Julia Wolleb, Robin Sandkühler, and Philippe C Cattin. DESCARGAN: Disease-specific anomaly detection with weak supervision. In *International Conference on Medical Image Computing and Computer-Assisted Intervention*, pages 14–24. Springer, 2020.
- [21] Md Mahfuzur Rahman Siddiquee, Zongwei Zhou, Nima Tajbakhsh, Ruibin Feng, Michael B Gotway, Yoshua Bengio, and Jianming Liang. Learning fixed points in generative adversarial networks: From image-to-image translation to disease detection and localization. In *Proceedings of the IEEE/CVF International Conference on Computer Vision*, pages 191–200, 2019.
- [22] Christoph Baur, Robert Graf, Benedikt Wiestler, Shadi Albarqouni, and Nassir Navab. SteGANomaly: Inhibiting CycleGAN steganography for unsupervised anomaly detection in brain MRI. In *International Conference on Medical Image Computing and Computer-Assisted Intervention*, pages 718–727. Springer, 2020.
- [23] Junlin Han, Mehrdad Shoeiby, Lars Petersson, and Mohammad Ali Armin. Dual contrastive learning for unsupervised image-to-image translation. In *Proceedings of the IEEE/CVF Conference on Computer Vision and Pattern Recognition*, pages 746–755, 2021.
- [24] Yanwu Xu, Shaoan Xie, Wenhao Wu, Kun Zhang, Mingming Gong, and Kayhan Batmanghelich. Maximum spatial perturbation consistency for unpaired image-to-image translation. *arXiv preprint:2203.12707*, 2022.

- [25] Jaewoong Choi, Daeha Kim, and Byung Cheol Song. Style-guided and disentangled representation for robust image-to-image translation. 2022.
- [26] Fangneng Zhan, Yingchen Yu, Rongliang Wu, Jiahui Zhang, Shijian Lu, and Changgong Zhang. Marginal contrastive correspondence for guided image generation. In *Proceedings of the IEEE/CVF Conference on Computer Vision and Pattern Recognition*, pages 10663–10672, 2022.
- [27] Chanyong Jung, Gihyun Kwon, and Jong Chul Ye. Exploring patch-wise semantic relation for contrastive learning in image-to-image translation tasks. In *Proceedings of the IEEE/CVF Conference on Computer Vision and Pattern Recognition*, pages 18260–18269, 2022.
- [28] Moab Arar, Yiftach Ginger, Dov Danon, Amit H Bermano, and Daniel Cohen-Or. Unsupervised multi-modal image registration via geometry preserving image-to-image translation. In *Proceedings of the IEEE/CVF conference on computer vision and pattern recognition*, pages 13410–13419, 2020.
- [29] Lingke Kong, Chenyu Lian, Detian Huang, Yanle Hu, Qichao Zhou, et al. Breaking the dilemma of medical image-to-image translation. *Advances in Neural Information Processing Systems*, 34, 2021.
- [30] Qianye Yang, Nannan Li, Zixu Zhao, Xingyu Fan, Eric I Chang, Yan Xu, et al. MRI cross-modality image-to-image translation. *Scientific reports*, 10(1):1–18, 2020.
- [31] Zekang Chen, Jia Wei, and Rui Li. Unsupervised multi-modal medical image registration via discriminator-free image-to-image translation. *arXiv preprint:2204.13656*, 2022.
- [32] Yun Liu, Yu-Huan Wu, Yunfeng Ban, Huifang Wang, and Ming-Ming Cheng. Rethinking computer-aided tuberculosis diagnosis. In *Proceedings of the IEEE/CVF Conference on Computer Vision and Pattern Recognition*, pages 2646–2655, 2020.
- [33] Jingyu Liu, Jie Lian, and Yizhou Yu. ChestX-Det10: Chest X-ray dataset on detection of thoracic abnormalities. *arXiv preprint:2006.10550*, 2020.
- [34] Raghavendra Selvan, Erik B Dam, Nicki S Detlefsen, Sofus Rischel, Kaining Sheng, Mads Nielsen, and Akshay Pai. Lung segmentation from chest x-rays using variational data imputation. *arXiv preprint:2005.10052*, 2020.
- [35] Junji Shiraishi, Shigehiko Katsuragawa, Junpei Ikezoe, Tsuneo Matsumoto, Takeshi Kobayashi, Ken-ichi Komatsu, Mitate Matsui, Hiroshi Fujita, Yoshie Kodera, and Kunio Doi. Development of a digital image database for chest radiographs with and without a lung nodule: Receiver operating characteristic analysis of radiologists’ detection of pulmonary nodules. *American Journal of Roentgenology*, 174(1): 71–74, 2000.
- [36] Stefan Jaeger, Sema Candemir, Sameer Antani, Yi-Xiang J Wang, Pu-Xuan Lu, and George Thoma. Two public chest X-ray datasets for computer-aided screening of pulmonary diseases. *Quantitative imaging in medicine and surgery*, 4(6):475, 2014.
- [37] Olaf Ronneberger, Philipp Fischer, and Thomas Brox. U-net: Convolutional networks for biomedical image segmentation. In *International Conference on Medical image computing and computer-assisted intervention*, pages 234–241. Springer, 2015.
- [38] Phillip Isola, Jun-Yan Zhu, Tinghui Zhou, and Alexei A Efros. Image-to-image translation with conditional adversarial networks. In *Proceedings of the IEEE Conference on Computer Vision and Pattern Recognition*, pages 1125–1134, 2017.

- [39] Diederik P Kingma and Jimmy Ba. Adam: A method for stochastic optimization. *arXiv preprint:1412.6980*, 2014.